ACS Catalysis

Research Article

Cite This: ACS Catal. 2018, 8, 7141−7157

pubs.acs.org/acscatalysis

Mechanisms and Active Sites for C−O Bond Rupture within 2-Methyltetrahydrofuran over Ni, $Ni_{12}P_5$, and Ni_2P Catalysts

Megan E. Witzke,[†] Abdulrahman Almithn,[‡] Christian L. Coonrod,[†] David D. Hibbitts,*[,‡] and David W. Flaherty*[,†]

[†]Department of Chemical and Biomolecular Engineering, University of Illinois Urbana−Champaign, Urbana, Illinois 61801, United States

[‡]Department of Chemical Engineering, University of Florida, Gainesville, Florida 32611, United States

Supporting Information

ABSTRACT: Nickel phosphide catalysts ($Ni_{12}P_5$ and Ni_2P) preferentially cleave sterically hindered ^{3}C−O bonds over unhindered ^{2}C−O bonds, and Ni_2P is up to 50 times more selective toward ^{3}C−O bond cleavage than Ni. Here, we combine kinetic measurements, in situ infrared spectroscopy, and density functional theory (DFT) calculations to describe the mechanism for C−O bond rupture over Ni, $Ni_{12}P_5$, and Ni_2P catalysts. Steady-state rate measurements and DFT calculations of C−O bond rupture within 2-methyltetrahydrofuran (MTHF) show that quasi-equilibrated MTHF adsorption and dehydrogenation steps precede kinetically relevant C−O bond rupture at these conditions (1−50 kPa MTHF; 0.1−6 MPa H_2; 543 K). Rates for ^{3}C−O and ^{2}C−O bond rupture are inhibited by H_2, and the ratio of these rates increases with $[H_2]^{1/2}$, suggesting that the composition of the reactive intermediates for ^{3}C−O and ^{2}C−O rupture differs by one H atom. Site-blocking CO*, NH_3*, and H* inhibit rates without altering the ratio of ^{3}C−O to ^{2}C−O bond rupture, indicating that these C−O bond rupture precursors and transition states bind to identical active sites. DFT-based predictions suggest that these sites are exposed ensembles of 3 Ni atoms on Ni(111) and $Ni_2P(001)$ and 4 Ni atoms on $Ni_{12}P_5(001)$ and that the incorporation of P disrupts extended Ni ensembles and alters the reactivity of the Ni. Increasing the phosphorus to nickel ratio (P:Ni) decreases measured and DFT-predicted activation enthalpies ($\Delta H^{\ddagger}$, 473−583 K) for ^{3}C−O bond rupture relative to that of ^{2}C−O bond rupture. Selectivity differences between specific C−O bonds within MTHF reflect differences in the H content of reactive intermediates, activation enthalpy barriers, and P:Ni of Ni, $Ni_{12}P_5$, and Ni_2P nanoparticles.

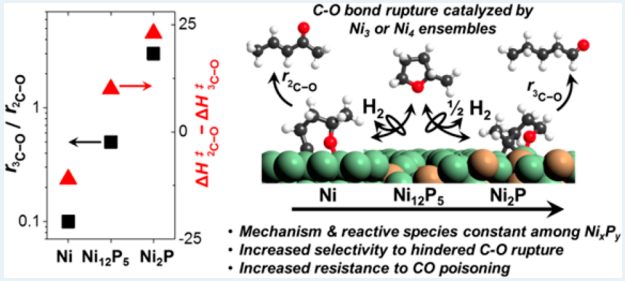

KEYWORDS: *nickel phosphide, reaction mechanism, hydrogenolysis, kinetics, 2-methyltetrahydrofuran, active site, DFT*

1. INTRODUCTION

Abundant amounts of unused, inedible biomass (e.g., corn stover, wood clippings) could be used as feedstocks for platform chemicals (e.g., benzene, α,ω-diols) that are traditionally synthesized from petroleum feeds, without competing with food sources.[1] Their high lignin content renders them difficult to process through microbial decomposition;[2] however, pyrolysis can depolymerize lignin into mixtures of smaller oxygenates (i.e., bio-oil).[1−3] Conversion of oxygenates (e.g., alcohols, ketones, furans, pyrans, and aromatics) into higher value chemicals (e.g., benzene, and α,ω-diols) requires cleavage of C−O bonds at select locations within these species to minimize hydrogen consumption and increase yield to high-value chemicals.[3−6] Yet, the selective rupture of specific C−O bonds without complete deoxygenation or competing C−C bond cleavage remains a challenge.[3,4,7]

Metal phosphides (MPs) are promising catalysts for selective C−O bond rupture. These materials were originally studied as catalysts for hydrodesulfurization and hydrodenitrogenation of fuels in response to increasingly stringent regulations on SO_x and NO_x emissions.[8−10] MPs selectively cleave C−(O,N,S) bonds over C−C bonds in comparison to transition metals,[11,12] metal sulfides,[9,13] and metal nitrides.[14] Previous studies have reported that selectivities and rates for C−O bond rupture change with the metal identity,[11,15−17] metal to phosphorus ratio (i.e., phosphide phase),[12,16,18] formation of bimetallic phosphides,[19−22] and variations in the support.[23−25] The reactivity of MPs for hydrogenolysis of C−O bonds in various oxygenates (e.g., anisole,[19] guaiacol,[17,18,23,25,26] 2-methyltetrahydrofuran (MTHF),[11,20,27−30] dibenzofuran,[16] and methyl laurate[21,24]) indicate that Ni_2P is the most reactive of the MPs studied (Ni_2P,[17,19,20,23,24,26−29] NiMoP,[19,21,31] MoP,[11,15,19,21] Fe_2P,[11,17,19,20] NiFeP,[20] Co_2P,[11,17] and WP[11,17]).

Received: December 20, 2017
Revised: June 14, 2018
Published: June 25, 2018

DOI: 10.1021/acscatal.7b04403
ACS Catal. 2018, 8, 7141−7157

While studies have shown Ni_2P has high selectivity and reactivity toward C−O bond rupture products, the mechanism toward specific C−O bond rupture (e.g., either at sterically hindered or unhindered positions) and the structure and functions of the active site remain unclear. The kinetics of MTHF over Ni_2P have been studied by analysis of rate data with a model derived for a mechanism considering multiple reactive intermediates for total deoxygenation;[27−30] however, models that specifically describe the rupture of each of the two C−O bonds have not been proposed previously. The heterogeneous surface of Ni_2P presents multiple potential active sites each of which may cleave hindered and unhindered C−O bonds; however, the identity of the active site (or sites) for these competing pathways has not been determined on these complex surfaces. Consequently, the relationship between MP properties and C−O bond cleavage selectivity is largely unclear.

In this study, we analyze two parallel mechanisms for C−O bond rupture in MTHF over supported Ni_2P, $Ni_{12}P_5$, and Ni catalysts using kinetic analysis, in situ spectroscopy, and density functional theory (DFT) calculations to identify the composition of the reactive intermediates and the active sites that bind them. Steady-state rate measurements obtained as a function of MTHF pressure ([MTHF], 1−50 kPa) and H_2 pressure ([H_2], 0.1−6 MPa) at 543 K show that adsorption and MTHF dehydrogenation steps are quasi-equilibrated, that the kinetically relevant step involves partially dehydrogenated intermediates, and that the active sites for this reaction on Ni, $Ni_{12}P_5$, and Ni_2P are largely covered by a mixture of MTHF-derived intermediates, CO*, and H*. DFT calculations confirm that C−O bond cleavage occurs after C−H bond activation of the carbon atom on Ni, $Ni_{12}P_5$, and Ni_2P surfaces. Thus, the mechanism for rupturing C−O bonds of MTHF strongly resembles those for C−C bond rupture in alkanes[32−34] and cycloalkanes[33] as well as C−O bond rupture in cyclic ethers[5] and alcohols[35] on transition metal surfaces. Rates of unhindered (^{2}C−O) and hindered (^{3}C−O) bond rupture are similarly inhibited by CO and NH_3 on Ni, $Ni_{12}P_5$, and Ni_2P catalysts, which suggests that both reactions occur at the same active site and that this active site also binds CO* and NH_3*. The H_2 dependencies of ^{3}C−O and ^{2}C−O bond rupture rates differ by $[H_2]^{1/2}$ on Ni, $Ni_{12}P_5$, and Ni_2P nanoparticles, which suggests that the transition state for ^{3}C−O bond cleavage has one more H atom than that for ^{2}C−O bond cleavage. Thus, both C−O ruptures occur after the complete dehydrogenation of the C atom involved. Measured and predicted activation enthalpies indicate lower activation enthalpies for ^{3}C−O relative to ^{2}C−O bond rupture with increased phosphorus to nickel ratios (P:Ni), which results in higher selectivity toward ^{3}C−O bond rupture over $Ni_{12}P_5$ and Ni_2P surfaces. Understanding the underlying reasons for these differences in reactivity and developing P-modified catalysts to selectively cleave hindered C−O (or other carbon bonds) within hydrogenolysis reaction networks would be desirable for the production of linear alcohols or diols from renewable biomass-derived feedstocks[5,36] and for the production of normal alkanes during ring-opening catalysis[37] and reforming of petrochemicals.[38]

2. RESULTS AND DISCUSSION

2.1. Selectivity for C−O Bond Cleavage. Figure 1 displays product selectivities for the reaction of MTHF with H_2 on SiO_2-supported 19 nm $Ni_{12}P_5$ nanoparticles as a function of conversion, which was controlled by varying the residence time of the reactant mixture (5 kPa MTHF, 1.0 MPa H_2, 543 K). Pentanal and 2-penten-4-one are the sole primary products of this reaction as shown by their nonzero selectivities (60% and 20%, respectively) as the conversion approaches zero (Figure 1a). The selectivities for all other products approach zero at short residence times (Figure 1b and 1c), which indicates that they are formed by secondary reactions. Pentanal and 2-penten-4-one form following rupture of the ^{3}C−O and the ^{2}C−O bonds, respectively, concurrent with C−H rupture and formation (Scheme 1). Figure 1b shows the secondary products that react at short residence times (i.e., at conversions below 0.3%) to form tertiary products. Secondary products, such as 1-pentanol, 2-penten-4-ol, 2-pentanone, and 2-pentanol, form by subsequent hydrogenation of pentanal and 2-penten-4-one (i.e., the primary products), whereas 1-butene and *n*-butane likely form by decarbonylation of pentanal and subsequent hydrogen transfer steps as indicated by formation

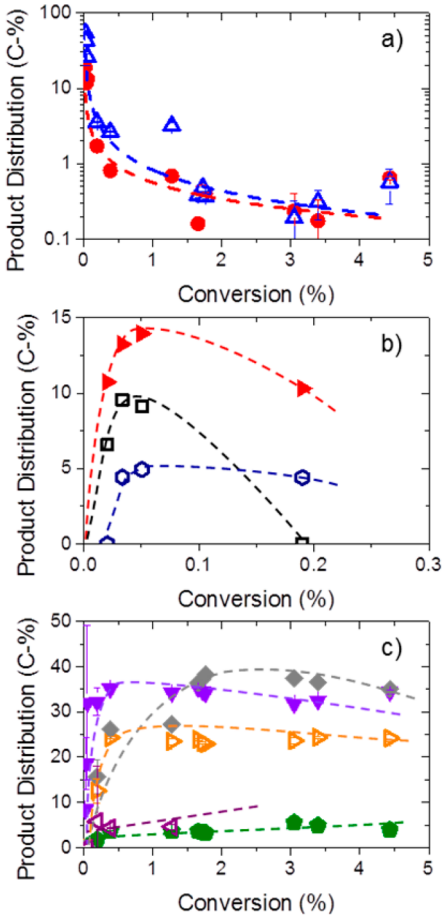

Figure 1. Selectivities toward primary C−O bond rupture products (a): pentanal (blue open triangles) and 2-penten-4-one (red solid circles); secondary products (b and c) formed by subsequent C−C or C−O bond rupture or hydrogenations including *n*-butane (orange open right-facing triangles), 1-butene (black open squares), *n*-pentane (green solid pentagons), 2-penten-4-ol (red solid right-facing triangles), 2-pentanone (purple solid down-facing triangles), 2-pentanol (gray diamonds), 1-pentanol (blue open hexagons), and carbon monoxide (purple open left-facing triangles) over 19 nm $Ni_{12}P_5$−SiO_2 at 5 kPa MTHF, 1 MPa H_2, and 543 K. Remaining products sum to less than 1% of product distribution. Lines are drawn to guide the eye. Selectivity data for 12 nm Ni_2P, 5 nm $Ni_{12}P_5$, and 4 nm Ni are shown in Supporting Information (Figure S1).

DOI: 10.1021/acscatal.7b04403
ACS Catal. 2018, 8, 7141−7157

Scheme 1. Proposed Pathways for Hydrogenolysis Reactions of MTHF over Supported Ni, $Ni_{12}P_5$, and Ni_2P Nanoparticles Based on Product Selectivities Reported in Figures 1 and S1

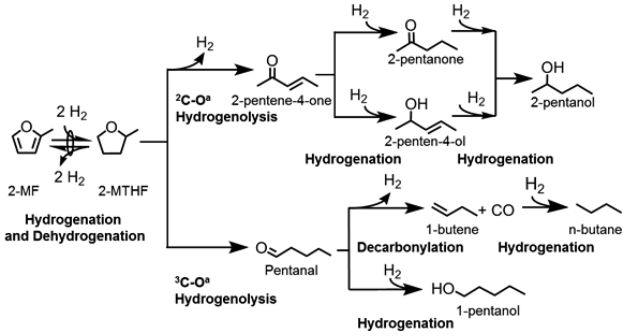

[a]The superscript (m in ^{m}C−O) indicates the number of C and O atoms bound to the ^{m}C atom.

of CO in nearly equimolar quantities (e.g., 23 ± 1 C-% selectivity to *n*-butane and 6 ± 1 C-% selectivity to CO at 1.2% conversion). Water forms from dehydrating 1-pentanol and 2-pentanol but is not indicated in Figure 1 because it lacks carbon. Figure S1 shows that selectivity patterns for hydrogenolysis on 5 nm $Ni_{12}P_5$ are similar to that on 19 nm $Ni_{12}P_5$, while 12 nm Ni_2P is highly selective toward pentane (80 C-%) and 4 nm Ni produces significantly less ^{3}C−O bond rupture products (e.g., *n*-butane and 1-pentanol). Pentane forms from the dehydration of 1- and 2-pentanol and, therefore, is not attributed to either pathway in calculations for turnover rates. Selectivities toward unsubstituted cyclic ethers (i.e., tetrahydrofuran and furan) or aliphatic ethers (e.g., diethyl ether and methyl propyl ether) are insignificant (i.e., < 0.1%) at the conditions of this study (473−575 K, 5 kPa MTHF, 1 MPa H_2, Figure S2), which demonstrates $Ni_{12}P_5$ predominantly cleaves C−O bonds (as opposed to C−C bonds) in primary reactions of MTHF. The lack of C−C cleavage in MTHF and the subsequent decarbonylation of pentanal is additional evidence that decarbonylation reactions occur via mechanisms distinct from C−C hydrogenolysis, as previously reported on Ir.[35]

Measured turnover rates for ^{2}C−O bond rupture (r_{2C-O}) and ^{3}C−O bond rupture (r_{3C-O}) (i.e., the consumption rate of MTHF to form 2-penten-4-one and subsequent ^{2}C−O bond rupture products, and pentanal and subsequent ^{3}C−O bond rupture products, respectively) decrease with increasing conversion to an extent much greater than expected based on depletion of the reactant (e.g., 40% decrease at less than 4% conversion) as demonstrated on 5 nm $Ni_{12}P_5$ (Figures S3a and S4; 0−5 kPa CO, 5 kPa MTHF, 1 MPa H_2, 543 K). These results suggest that a reaction product inhibits C−O bond rupture. CO is formed by decarbonylation of aldehyde products[27−30] (Figure 1, Scheme 1) and binds strongly to the catalyst surface, as shown by in situ FTIR measurements that reflect significant coverages of CO* on SiO_2-supported Ni_2P during reactions of H_2 and preadsorbed MTHF at 523 K.[28] Rates for C−O bond rupture are less affected by conversion as CO is cofed (0−5 kPa CO, Figure S3b), because the pressure of CO becomes a weak function of conversion. These data (Figure S3) indicate that r_{3C-O} and r_{2C-O} remain nearly constant over the range of differential MTHF conversion (at values < 10%) at CO pressures ([CO]) equal to or greater than 1 kPa CO and indicate that water formed from dehydrating alcohols (<0.05 kPa) is not responsible for product inhibition. Consequently, rate measurements made in the remainder of this paper were obtained (unless otherwise noted) with at least 1 kPa CO cofed.

Controlling C−O bond hydrogenolysis selectivity within MTHF and other oxygenates provides catalytic routes to produce value-added chemicals, such as cleaving hindered C−O bonds to produce α,ω-functionalized alcohols and aldehydes from 2-hydroxymethyl-tetrahydrofuran.[5] The ratio of the rate of r_{3C-O} to r_{2C-O} can be defined as follows

$$\chi = \frac{r_{^3C-O}}{r_{^2C-O}} \quad (1)$$

such that large values of χ demonstrate a preference for cleaving ^{3}C−O bonds. Values of χ depend weakly on conversion in the absence of cofed CO (Figure 2, 1 MPa H_2, 5 kPa MTHF, 543 K) over SiO_2-supported Ni, $Ni_{12}P_5$, and Ni_2P nanoparticles, which suggests that both r_{2C-O} and r_{3C-O} are similarly inhibited by CO. Values of χ increase systematically with increasing bulk ratio of atomic phosphorus to atomic nickel (P:Ni) among these catalysts; χ values are 50 times greater on Ni_2P than on Ni, which suggests Ni_2P may be preferred over Ni for hydrogenolysis of substituted furanic and pyranic compounds found in bio-oil. These differences in product selectivities suggest that the inclusion of phosphorus within the $Ni_{12}P_5$ and Ni_2P nanoparticles alters the mechanism for C−O bond rupture, the identity of the active site, or the underlying enthalpy and free energy barriers for these reactions. The reasons for these selectivity differences have not been fully resolved in previous publications that analyze C−O bond rupture in various ethers over SiO_2-supported MPs.[11,17−19,21,27−30] $Ni_{12}P_5$ and Ni_2P nanoparticles show higher selectivity toward ^{3}C−O bond rupture compared with Ni, and the following sections identify the underlying mechanism and active sites responsible for C−O bond rupture and explain this selectivity difference.

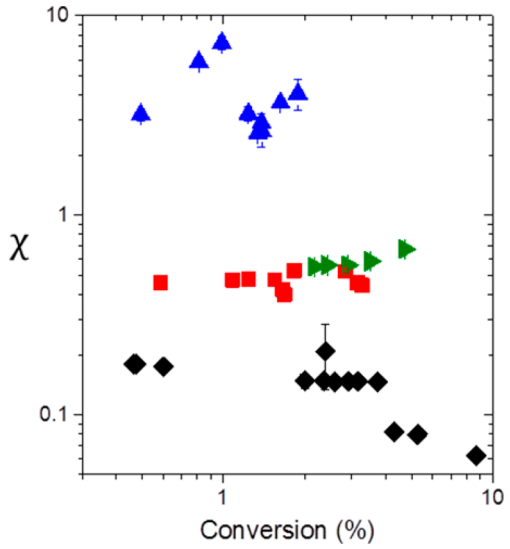

Figure 2. Ratio of ^{3}C−O to ^{2}C−O bond rupture rates (χ) for 4 nm Ni (black diamonds), 5 nm $Ni_{12}P_5$ (green triangles), 19 nm $Ni_{12}P_5$ (red squares), and 12 nm Ni_2P (blue triangles) at 1 MPa H_2, 5 kPa MTHF, 543 K.

DOI: 10.1021/acscatal.7b04403
ACS Catal. 2018, 8, 7141−7157

2.2. Effects of Reactant Pressures on C−O Bond Rupture Rates on Ni, $Ni_{12}P_5$, and Ni_2P Catalysts. C−H bonds can break and form rapidly at reaction conditions that favor C−O and C−C bond rupture in alkanes and alcohols as shown previously,[5,33,35] and this also occurs here through the dehydrogenation of MTHF to 2-methylfuran (MF) illustrated in Scheme 1. The approach to equilibrium (η) for the dehydrogenation of MTHF is defined as follows

$$\eta = \frac{[H_2]^2 \cdot [MF]}{K_{DH} \cdot [MTHF]} \quad (2)$$

where K_{DH} is the equilibrium constant for dehydrogenation. Figure S5 shows that η is nearly unity and does not depend on residence time or reactant conversion on all catalysts (1−50 kPa MTHF, 250−500 kPa H_2, 1−2.5 kPa CO, 543 K), which indicates that MTHF dehydrogenation is quasi-equilibrated at all conditions of this study. By extension, we assume that partially dehydrogenated surface and gaseous intermediates derived from MTHF exist within a quasi-equilibrated pool of reactants, referenced hereafter as the MTHF-MF reactant pool.

C−O bond rupture turnover rates increase with increasing [MTHF] but become less sensitive to [MTHF] at higher pressures in ways that likely reflect increases in the surface coverages of MTHF-derived intermediates (Figure 3, 250−500 kPa H_2, 1−2.5 kPa CO, 543 K). Similar rate dependencies were described on Ni_2P-SiO_2 at comparable conditions (332 kPa H_2, 573 K).[30] These effects of [MTHF] on reaction rates closely follow predictions from a simple first-order Langmuir−Hinshelwood rate equation (Section S1). Increasing coverage of MTHF-derived intermediates also indicates that these intermediates can compete with adsorbed CO (CO*), which covers active sites at these conditions, as suggested by strong inhibition by CO at these pressures (Figure S3).

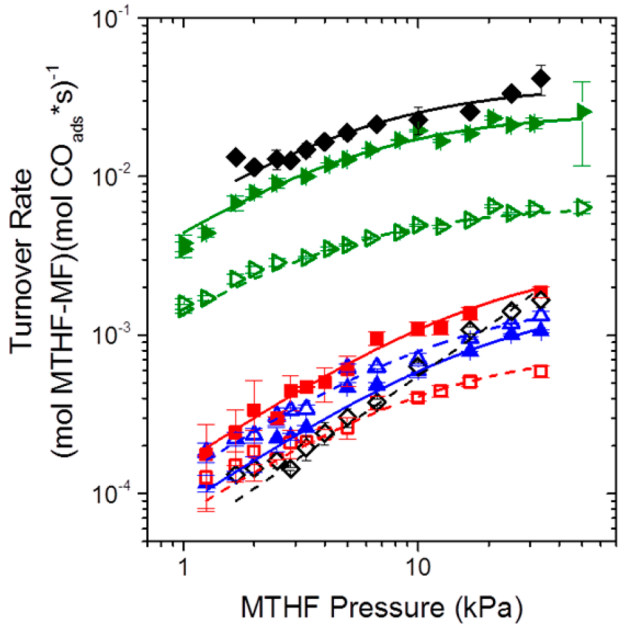

Figure 3. Changes in rates of consumption of the MTHF-MF reactant pool to form pentanal and subsequent ^{3}C−O bond rupture products (open symbols) and 2-penten-4-one and subsequent ^{2}C−O bond rupture products (solid symbols) indicated in Scheme 1 as functions of MTHF pressure in the presence of CO over 4 nm Ni (black diamonds, 2.5 kPa CO, 500 kPa H_2), 5 nm $Ni_{12}P_5$ (green triangles, 1 kPa CO, 250 kPa H_2), 19 nm $Ni_{12}P_5$ (red squares, 2.5 kPa CO, 500 kPa H_2), and 12 nm Ni_2P (blue triangles, 2.5 kPa CO, 500 kPa H_2) at 543 K. Trend lines reflect fits to an inhibited, unimolecular, Langmuir−Hinshelwood expression (Section S1). Figure S6 displays these data as total turnover rates and selectivities.

In situ vibrational spectroscopy can provide direct evidence for the identity of surface species present during C−O bond rupture on $Ni_{12}P_5$ and Ni_2P surfaces. In situ FTIR spectra (Figure S7) obtained during reactions of MTHF with H_2 over Ni, $Ni_{12}P_5$, and Ni_2P catalysts (5 kPa MTHF, 81 kPa H_2, 543 K) show a combination of spectral features between 3000 and 2700 cm^{-1} attributed to asymmetric and symmetric $\nu(CH_x)$ modes.[39−41] These $\nu(CH_x)$ modes correspond only to surface intermediates derived from MTHF on Ni, $Ni_{12}P_5$, and Ni_2P as the intensities of surface intermediates on SiO_2 are negligible, and the gas-phase contributions of MTHF have been subtracted. CO formed by decarbonylation of reaction intermediates bind to $Ni_{12}P_5$ and Ni surfaces at these conditions, as shown by distinct absorbance features at 2035 cm^{-1} on $Ni_{12}P_5$ and in the range of 1710−2025 cm^{-1} on Ni that correspond to reported frequencies for CO bound to Ni ensembles on Ni_2P[28] and Ni surfaces,[42,43] respectively, and which shows that CO formed by decarbonylation of reaction intermediates produces CO partial pressures that are sufficiently high to compete with MTHF-derived species for active sites. Additional spectra of adsorbed CO over Ni are shown in the Supporting Information (Figure S8). The lack of an obvious absorbance feature for ν(CO) on 12 nm Ni_2P indicates that CO* exists at much lower coverages on the Ni_2P surface relative to the Ni and $Ni_{12}P_5$ surfaces at these conditions, which is consistent with binding energies for CO* on Ru(0001) that decrease as the ratio of atomic phosphorus to ruthenium increases.[44] The coexistence of CO* and MTHF-derived surface intermediates (Figure S7) is consistent with product inhibition from CO (Figures S3 and S4), the form of the rate dependence on [MTHF] (Figure 3), and previous spectroscopic observations of coadsorbed MTHF and CO formed in situ over Ni_2P nanoparticles.[28]

Both r_{2C-O} and r_{3C-O} decrease upon cofeeding increasing [CO] over all Ni, $Ni_{12}P_5$, and Ni_2P nanoparticles (Figure 4, 5 kPa MTHF, 0.25−1 MPa H_2, 543 K), which confirms that the CO* binds to active sites for ^{3}C−O and ^{2}C−O bond rupture. The degree of CO inhibition on C−O bond rupture rates decreases with increasing molar ratio of P to Ni, with Ni catalysts being most sensitive to [CO] ($r_{C-O} \sim [CO]^{-1.5}$), while $Ni_{12}P_5$ (both 5 and 19 nm) is less so ($r_{C-O} \sim [CO]^{-1}$), and Ni_2P is nearly unaffected ($r_{C-O} \sim [CO]^{-0.2}$), which agrees with the relative sizes of CO* features within in situ FTIR spectra (Figure S7). Thus, CO (produced either in situ or cofed) adsorbs to active sites for C−O bond rupture in competition with MTHF-derived intermediates and binds less strongly to Ni_2P surfaces than to either $Ni_{12}P_5$ or Ni surfaces. The lower proclivity for CO to bind to and inhibit reactions on phosphorus-modified Ni catalysts resembles similar trends shown by studies of temperature-programmed desorption of CO from phosphorus-modified Ni(100) surfaces.[45] These investigations demonstrated that the sticking coefficient of CO decreases with increasing P coverage, because the presence of electronegative P atoms decreased the extent of back-donation from the Ni atoms to the adsorbed CO.[45] The resistance of Ni_2P surfaces to CO poisoning expands the benefits of $Ni_{12}P_5$ and Ni_2P as hydrogenolysis catalysts. On all catalysts, CO inhibits both ^{3}C−O and ^{2}C−O bond rupture to the same

DOI: 10.1021/acscatal.7b04403
ACS Catal. 2018, 8, 7141−7157

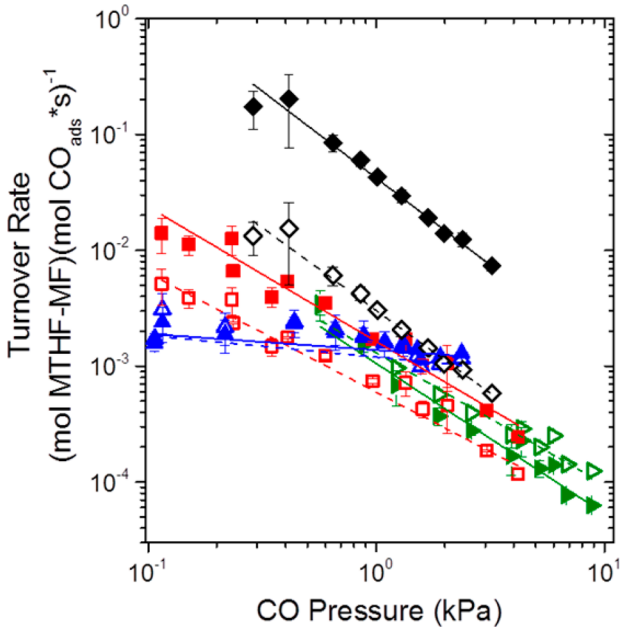

Figure 4. Change in rates of consumption of the MTHF-MF reactant pool to form pentanal and subsequent ^{3}C−O bond rupture products (open symbols) and 2-penten-4-one and subsequent ^{2}C−O bond rupture products (solid symbols) indicated in Scheme 1 as functions of CO pressure over 4 nm Ni (black diamonds, 0.5 MPa H_2), 5 nm-$Ni_{12}P_5$ (green triangles, 1 MPa H_2), 19 nm-$Ni_{12}P_5$ (red squares, 0.5 MPa H_2), and Ni_2P (blue triangles, 0.25 MPa H_2) in 5 kPa MTHF at 543 K. Trend lines indicate power law fits. Figure S8 displays these data as total turnover rates and selectivities.

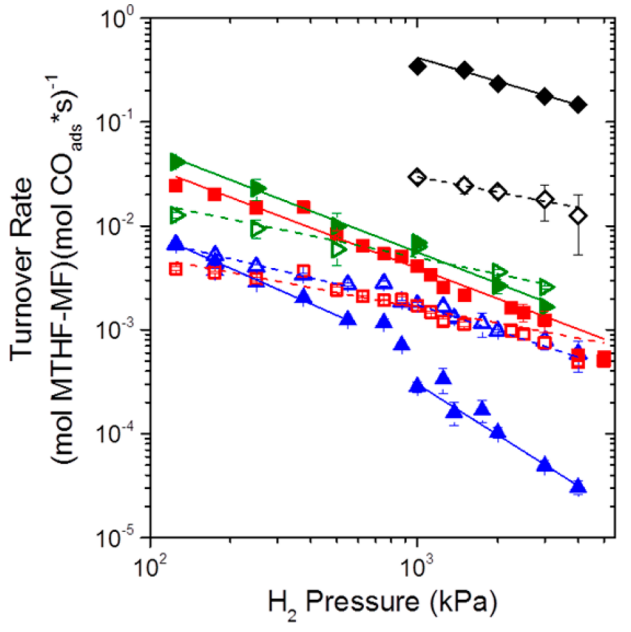

Figure 5. Change in rates of consumption of the MTHF-MF reactant pool to form pentanal and subsequent ^{3}C−O bond rupture products (open symbols) and 2-penten-4-one and subsequent ^{2}C−O bond rupture products (solid symbols) indicated in Scheme 1 as functions of H_2 pressure over 4 nm Ni (black diamonds), 5 nm $Ni_{12}P_5$ (green triangles), 19 nm $Ni_{12}P_5$ (red squares), and 12 nm Ni_2P (blue triangles) in 5 kPa MTHF at 543 K. Trend lines represent fits to power law equation. Figure S10 displays these data as total turnover rates and selectivities.

extent (Figure 4), suggesting that both reactions occur at the same active site regardless of the surface composition or structure.

Measured r_{2C-O} and r_{3C-O} values decrease with increasing $[H_2]$ on Ni, $Ni_{12}P_5$, and Ni_2P catalysts (Figure 5). On $Ni_{12}P_5$ and Ni, ^{2}C−O bond rupture shows an inverse first-order dependence in $[H_2]$ (i.e., $r_{2C-O} \sim [H_2]^{-1}$), while ^{3}C−O bond rupture shows an inverse half-order dependence (i.e., $r_{3C-O} \sim [H_2]^{-1/2}$). H_2 kinetics for Ni_2P are similar to those on $Ni_{12}P_5$ and Ni at moderate H_2 pressures (<0.75 MPa H_2), but rates are more inhibited by H_2 ($r_{2C-O} \sim [H_2]^{-3/2}$ and $r_{3C-O} \sim [H_2]^{-1}$) at higher pressures. Differences in the degree of H_2 inhibition toward ^{2}C−O and ^{3}C−O bond rupture leads to χ values that increase with a half-order dependence on $[H_2]$ (i.e., $\chi \sim [H_2]^{1/2}$). Hydrodeoxygenation rates for MTHF are reported to increase with $[H_2]$ for Ni_2P on USY at 573 K[29] and decrease with $[H_2]$ ($r \sim [H_2]^{-1/2}$) for Ni_2P supported on SiO_2.[28] Yet neither of these publications report turnover rates for ^{2}C−O and ^{3}C−O bond rupture specifically. Related investigations of C−C bond rupture rates in hydrocarbons[32−34] and C−O bond rupture in oxygenates[5,35] on transition metal catalysts have shown that C−C or C−O bonds cleave in dehydrogenated species, which cause r_{C-C} and r_{C-O} to depend on $[H_2]$ in ways that reflect the total number of H atoms removed from the reactant and the catalyst surface in quasi-equilibrated steps preceding C−C or C−O bond rupture. The independence of χ as CO* coverage changes (Figure 4), however, indicates that ^{2}C−O and ^{3}C−O bond rupture occurs on identical sites, which shows that the effect of $[H_2]$ on χ values must originate from differences in the H content of their transition states instead of differences in the amount of displaced H*. These data, taken together, suggest that the transition states which mediate ^{2}C−O bond rupture are more deeply dehydrogenated (by one H atom) than those which mediate ^{3}C−O bond rupture. Similarly, the composition of active intermediates for ^{2}C−^{2}C bond rupture are more dehydrogenated by one H atom than ^{3}C−^{2}C bond rupture in cycloalkanes over supported Ir, Ru, Rh, and Pt catalysts as ^{2}C must lose two H atoms while ^{3}C only loses a single H atom.[33] The observed surface species and effects on $[H_2]$, [MTHF], and [CO] suggest that C−O bond rupture occurs in oxygenate intermediates following quasi-equilibrated C−H bond cleavage.

2.3. Proposed Elementary Steps and Derived Rate Expression. Scheme 2 shows a series of elementary steps that lead to C−O bond rupture within MTHF on Ni, $Ni_{12}P_5$, and Ni_2P catalysts. These steps and their assumed reversibilities lead to rate equations that are consistent with the rate measurements shown in Figures 3, 4, and 5 and with the quasi-equilibrated adsorption and dehydrogenation of MTHF (i.e., $\eta \rightarrow 1$ in eq 2, Figure S5). Dissociative adsorption of H_2 to form H* (Step 2.0), molecular adsorption of MTHF (Step 2.1), and sequential dehydrogenation of the C atoms of the cleaved ^{2}C−O and ^{3}C−O bonds (Steps 2.2a, 2.3a, and 2.2b) are assumed to be quasi-equilibrated based on the observed quasi-equilibrated nature of MTHF dehydrogenation (Figure S5). The adsorption of CO (Step 2.6) is assumed to be quasi-equilibrated as effects of CO pressure on rates are fully reversible. The ruptures of ^{2}C−O (Step 2.4a) and ^{3}C−O (Step 2.3b) bonds are both sole kinetically relevant steps for the two pathways shown in Scheme 2, and the C atoms of these bonds are assumed to be fully dehydrogenated prior to C−O cleavage, based on the observed dependence of rates on

DOI: 10.1021/acscatal.7b04403
ACS Catal. 2018, 8, 7141−7157

Scheme 2. Proposed Elementary Steps for ^{2}C−O (2.1-2.5a) and ^{3}C−O (2.1-2.4b) Bond Rupture in MTHF on Ni_2P, $Ni_{12}P_5$, and Ni Nanoparticles

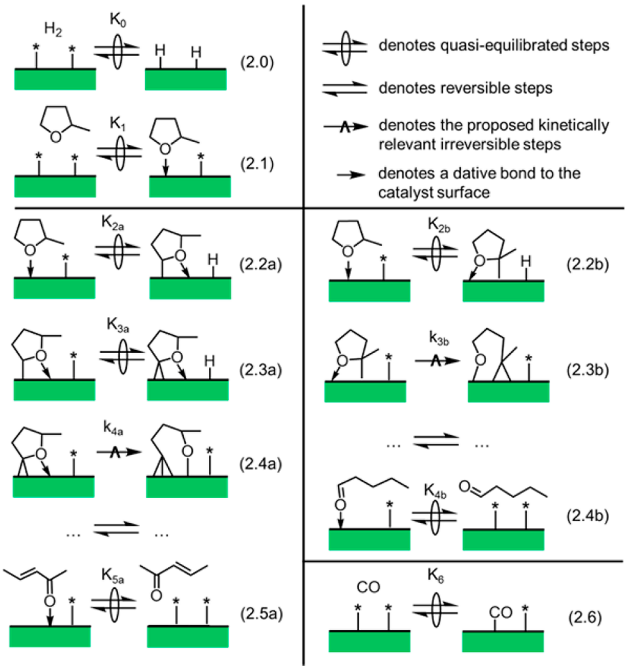

[H_2] (Figure 5). A series of steps follow the kinetically relevant steps (2.4a and 2.3b) to form the primary products, 2-pentene-4-one and pentanal, indicated in Figure 1. This mechanism provides physical understanding of C−O bond rupture, and the rate constants, both measured and calculated using DFT, provide additional insights and corroboration of this mechanism.

Intrinsic activation enthalpies (ΔH_{act}) and reaction enthalpies (ΔH_{rxn}) for C−O cleavage pathways within Scheme 2 and others were calculated using DFT to validate the proposed mechanisms and to estimate apparent activation enthalpies ($\Delta H^{\ddagger}$) for C−O bond rupture for comparisons to experimentally determined $\Delta H^{\ddagger}$ values (shown in section 2.5). Gaseous MTHF can adsorb and react with an unoccupied site on the $Ni_2P(001)$ surface to undergo ^{2}C−O bond cleavage (H_{act} = 140 kJ mol^{-1}) or ^{3}C−O bond cleavage (H_{act} = 139 kJ mol^{-1}) (Figure 6); however, these barriers are much greater than those to dehydrogenate the ^{2}C (H_{act} = 85 kJ mol^{-1}) or ^{3}C atoms (H_{act} = 111 kJ mol^{-1}). Similarly, the barrier to remove the second H atom from the ^{2}C atom (H_{act} = 71 kJ mol^{-1}) is lower than that for ^{2}C−O activation (H_{act} = 105 kJ mol^{-1}) of that intermediate. The number and lengths of the bonds that each calculated transition-state forms to the surface indicate that fully dehydrogenated intermediates are more strongly bound to the surface than partially dehydrogenated intermediates (Figure S11). Reverse barriers for C−H activation are lower than the forward barriers for C−O cleavage, consistent with quasi-equilibrated C−H cleavage. Comparisons between the barriers for C−H and C−O cleavage confirm that C atoms are fully dehydrogenated in a series of quasi-equilibrated steps prior to C−O bond rupture, which supports the mechanism proposed in Scheme 2 and the composition of the reactive intermediates inferred from kinetic data (section 2.2).

The activation enthalpy barriers relative to a bare $Ni_2P(001)$ surface ($\Delta H^{\ddagger}$) increase as MTHF is dehydrogenated (from 144 to 162 to 182 kJ mol^{-1} for ^{2}C−O cleavage and from 143 to 148 kJ mol^{-1} for ^{3}C−O cleavage), indicating that it is enthalpically easier to activate C−O bonds in less dehydrogenated intermediates. These transition states, however, differ in the number of quasi-equilibrated C−H activations that precede them, and each C−H activation in this series results in the formation of $^1/_2H_2$(g) because H_2 dissociation and reformation occur at rates much greater than C−O activation (i.e., Step 2.0 is quasi-equilibrated, as indicated by the equilibration between MTHF and MF at all conditions, Figure S5). Enthalpy barriers for C−O cleavage do not reflect the entropy gain upon dehydrogenation and subsequent H_2(g) formation, and these entropic effects will favor C−O cleavage in extensively dehydrogenated intermediates. Free-energy barriers ($\Delta G^{\ddagger}$) that appropriately account for entropy at relevant temperatures (543 K) show that C−O bond rupture in intermediates with fully dehydrogenated C atoms have the lowest $\Delta G^{\ddagger}$ values for both ^{2}C−O and ^{3}C−O cleavage (Figure

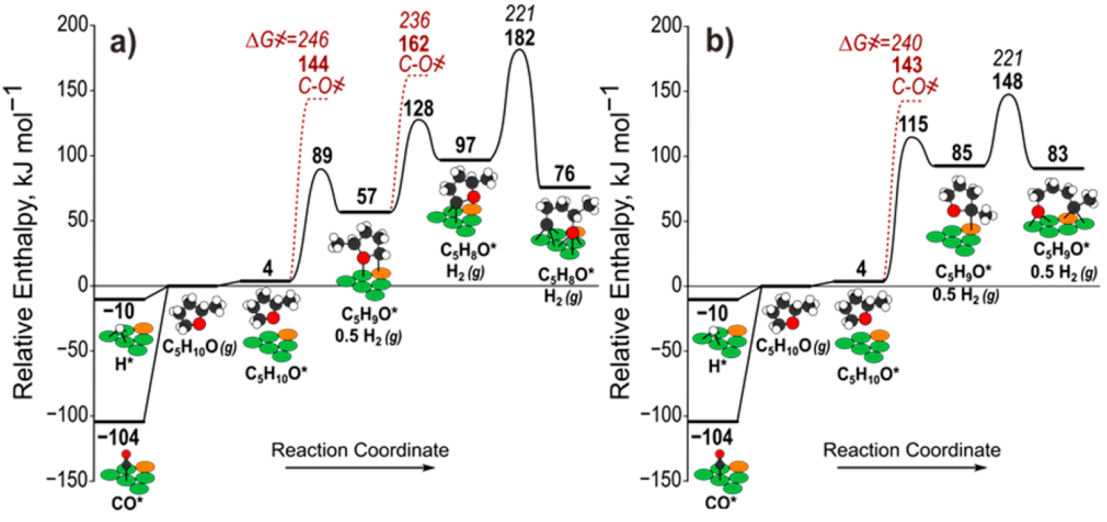

Figure 6. Reaction coordinate diagrams for changes in enthalpy in elementary steps that form the transition state for ^{2}C−O (a) and ^{3}C−O (b) bond rupture in MTHF on the $Ni_2P(001)$ surface at 543 K (O, red; C, black; H, white; P, orange; Ni, green). Dashed lines show barriers for unfavorable C−O bond activation. Overall free-energy barriers ($\Delta G^{\ddagger}$) for each C−O cleavage transition state are shown in italics.

DOI: 10.1021/acscatal.7b04403
ACS Catal. 2018, 8, 7141−7157

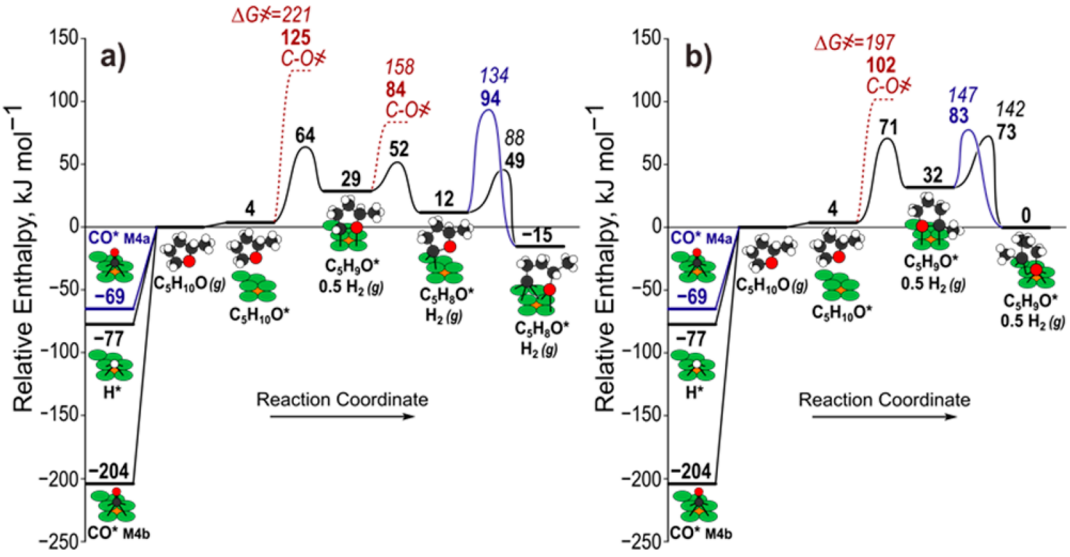

Figure 7. Reaction coordinate diagrams for changes in enthalpy in elementary steps that form the transition state for ^{2}C−O (a) and ^{3}C−O (b) bond rupture in MTHF on the $Ni_{12}P_5$(001) surface at 543 K (O, red; C, black; H, white; P, orange; Ni, green). Dashed lines show barriers for unfavorable C−O bond activation. Overall free-energy barriers ($\Delta G^{\ddagger}$) for each C−O cleavage transition state are shown in italics. C−O bond activation barriers on the $M4_a$ site are shown in blue.

6), which suggests that C−O cleavage occurs after complete dehydrogenation of the C atom, consistent with Scheme 2. The enthalpic preference for C−H cleavage over C−O cleavage, the entropic effects associated with dehydrogenation, and the preferential C−O cleavage following complete dehydrogenation of the C atom is also shown by DFT calculations on the $Ni_{12}P_5$ and Ni surfaces (Figures 7 and S12, respectively).

Scheme 2 indicates that rates of C−O bond rupture (r_{3C-O} and r_{2C-O}) are proportional to the concentration of the MTHF-derived reactive intermediates specific to each C−O bond rupture pathway

$$r_{^{m}C-O} = k_{^{m}C-O}[C_5H_{6+m}O^*] \quad (3)$$

Here, m is the number of C and O atoms the ^{m}C is bound to prior to ^{m}C−O bond rupture (i.e., 2 or 3) and $k_{^{m}C-O}$ is the intrinsic rate constant for ^{m}C−O bond rupture in $C_5H_{6+m}O^*$ intermediates derived from MTHF by quasi-equilibrated dehydrogenation steps (e.g., ^{2}C−O bonds cleave in $C_5H_8O^*$, which is formed by removing 2 H atoms from the ^{2}C atom). A rate expression for ^{m}C−O bond rupture in MTHF-derived intermediates is derived by applying the pseudo-steady-state hypothesis to $[C_5H_{6+m}O^*]$ and treating adsorption and dehydrogenation steps as quasi-equilibrated as prescribed by Scheme 2

$$r_{^{2}C-O} = k_{4a}\cdot K_{3a}\cdot K_{2a}\cdot K_1\cdot[MTHF]\cdot(K_0\cdot[H_2])^{-1}\cdot[*] \quad (4a)$$

$$r_{^{3}C-O} = k_{3b}\cdot K_{2b}\cdot K_1\cdot[MTHF]\cdot(K_0\cdot[H_2])^{-(1/2)}\cdot[*] \quad (4b)$$

where rate (k) and equilibrium (K) constants are defined in Scheme 2 and [*] is the concentration of unoccupied sites for ^{m}C−O bond rupture.

An expression for [*] is obtained by invoking a site balance for all potential surface species and applying the quasi-equilibrium assumptions as before

$$[L] = [*] + \sum_{i=0}^{n=4}\left(\left(\prod_{j=1}^{i} K_{CH,j}\right)\cdot[H_2]^{-(i/2)}\cdot K_1\cdot[MTHF]\cdot[*]\right) + (K_0\cdot[H_2])^{1/2}\cdot[*] + K_{CO}\cdot[CO]\cdot[*] \quad (5)$$

Here, $\prod_{j=1}^{i} K_{CH,j}$ is the product of equilibrium constants to form each sequential dehydrogenated MTHF-derived intermediate, j, leading to intermediate i, where i is the number of H atoms removed from MTHF. Here, we assume a single-site mechanism based on the similar site requirements for MTHF-derived intermediate, H atoms, and CO over $Ni_{12}P_5$ and Ni_2P catalysts (Figures 3, 4, and 5). The sublinear dependence on MTHF is consistent with the coexistence of MTHF-derived species and CO* as most abundant surface intermediates (MASI). The enthalpy differences between adsorbed MTHF ($C_5H_{10}O^*$) and the partially dehydrogenated species ($C_5H_{10-i}O^*$) that form via quasi-equilibrated C−H bond rupture (Figures 6 and 7) suggest that the coverage of $C_5H_{10}O^*$ (i.e., $K_1\cdot[MTHF]$) will be much greater than those of all dehydrogenated MTHF-derived species. This conclusion is also supported by reaction orders in $[H_2]$ for r_{3C-O} and r_{2C-O} that are constant from 1 to 4 MPa H_2 on Ni and from 0.125 to 6 MPa H_2 on $Ni_{12}P_5$ nanoparticles (Figure 5), which suggests that the H content and coverage of all MASI do not change in response to a near 50-fold increase in $[H_2]$. The decrease of the r_{3C-O} and r_{2C-O} dependence on $[H_2]$ by one-half order at $[H_2]$ greater than 0.75 MPa over 12 nm Ni_2P clusters (Figure 5) indicates that H* becomes the MASI at such conditions. These assertions on the nature of the MASI, along with eqs 4a, 4b, and 5, yield complete rate expressions for ^{m}C−O bond rupture in terms of gas-phase species

$$\frac{r_{^{2}C-O}}{[L]} = \frac{k_{4a}\cdot K_{3a}\cdot K_{2a}\cdot K_1\cdot[MTHF]\cdot(K_0\cdot[H_2])^{-1}}{(1 + K_1\cdot[MTHF] + (K_0\cdot[H_2])^{1/2} + K_{CO}\cdot[CO])} \quad (6a)$$

DOI: 10.1021/acscatal.7b04403
ACS Catal. 2018, 8, 7141−7157

$$\frac{r_{^3C-O}}{[L]} = \frac{k_{3b}\cdot K_{2b}\cdot K_1\cdot[\mathrm{MTHF}]\cdot(K_0\cdot[H_2])^{-(1/2)}}{(1 + K_1\cdot[\mathrm{MTHF}] + (K_0\cdot[H_2])^{1/2} + K_{CO}\cdot[CO])} \quad (6b)$$

These derived rate expressions account for the effects of [MTHF] (Figure 3), [H_2] (Figure 5), and [CO] (Figures 4, S3, and S4) on ^{m}C−O bond rupture rates during MTHF hydrogenolysis. The rate expressions in eqs 6a and 6b describe rates on all measured materials as shown by the comparison of measured turnover rates over a wide range of conditions (Figures 3−5) and predicted rates obtained by regression of rate constants for each material (Figure S13).

These experimental and computational results show that ^{2}C−O and ^{3}C−O bond rupture occurs in $C_5H_8O^*$ and $C_5H_9O^*$ species, respectively, following quasi-equilibrated dehydrogenation of the ^{m}C atom on surfaces covered by a mixture of CO*, $C_5H_{10}O^*$, and H*. Measurements and calculations described in section 2.4 further probe the chemical nature and the structure of the active sites for ^{3}C−O and ^{2}C−O bond rupture.

2.4. Identity and Chemical Nature of C−O Bond Rupture Active Sites. Figure 8 shows potential binding sites on Ni(111), $Ni_2P(001)$, and $Ni_{12}P_5(001)$ surfaces, and Figure 9 and Table S3 display the preferred binding sites and structures for the transition states and MASIs (i.e., CO*, H*, and $C_5H_{10}O^*$) calculated by DFT on Ni, $Ni_{12}P_5$, and Ni_2P surfaces. Transition-state structures and H* both bind at the 3-fold Ni hollow of $Ni_2P(001)$ (M_3), while the most stable adsorption site for CO* on $Ni_2P(001)$ is atop Ni (M_1). CO binds more weakly to $Ni_2P(001)$ (CO heat of adsorption, Q_{CO} = 104 kJ mol^{-1}) relative to Ni(111) and $Ni_{12}P_5(001)$ (142 and 204 kJ mol^{-1}, respectively), which is consistent with the weaker CO inhibition on Ni_2P nanoparticles ($r_{C-O} \sim [CO]^{-0.2}$, Figure 4) compared with Ni and $Ni_{12}P_5$ ($r_{C-O} \sim [CO]^{-1}$, Figure 4). H* becomes a MASI on Ni_2P at high [H_2] (>0.75 MPa H_2), but this does not occur on Ni or $Ni_{12}P_5$ surfaces (Figure 5). The increase in H* coverage on Ni_2P may be facilitated by the relatively low CO* coverages on that surface (compared to Ni or $Ni_{12}P_5$). In comparison, transition-state structures on the $Ni_{12}P_5(001)$ surface bind to the two different 4-fold Ni hollows at the center and corners of the unit cell (Figure 8, M_{4a} and M_{4b}). ^{2}C−O and ^{3}C−O bonds ruptures occur preferentially on the M_{4b} site, and ^{2}C−O bond rupture is 24 kJ mol^{-1} enthalpically more favorable than ^{3}C−O bond rupture (Figure 7), inconsistent with the measured enthalpy differences discussed in section 2.5; however, the M_{4b} site is also the preferred adsorption site for CO* on $Ni_{12}P_5(001)$ surface and has a significantly greater Q_{CO} relative to M_{4a} (Q_{CO} of 204 and 69 kJ mol^{-1}, respectively). The large values of Q_{CO} on M_{4b} sites suggest that CO* binds to those sites irreversibly, leaving M_{4a} sites to catalyze both pathways and leading to DFT-predicted $\Delta H^{\ddagger}$ values for C−O bond rupture pathways (Figure 7, blue) that are more consistent with the measured values, discussed in section 2.5. CO* bound irreversibly to $M4_b$ sites had little effect on the reactivity of M_{4a} sites, as shown by C−O cleavage calculations with a spectating CO* on M_{4b} (Figure S14).

DFT calculations predict Q_{CO} to be much larger than MTHF on all three surfaces (Table S3), which is consistent with the observation that even at low [CO] CO significantly inhibits C−O cleavage, as described in section 2.1. However, the small values of Q_{MTHF} are not consistent with the observed sublinear dependence of r_{C-O} on [MTHF] (Figure 3) or the spectroscopic evidence for the coexistence of $C_5H_{10}O^*$ and CO* during catalysis (Figure S7). Notably, the revised Perdew−Burke−Ernzerhof (RPBE) functional used here underestimates Q of physisorbed species, such as MTHF, because it does not account for attractive van der Waals

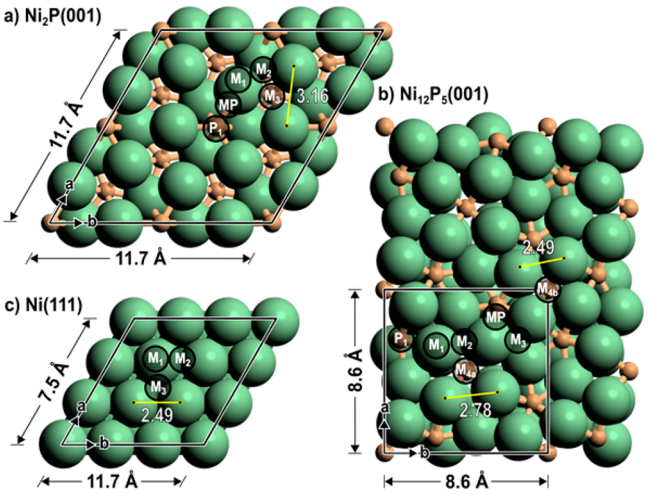

Figure 8. Top views of Ni_2P (a), $Ni_{12}P_5$ (b), and Ni (c) supercells. Adsorption sites to Ni (green) and P (orange) atoms are labeled as follows: M_1, metal atop; M_2, metal bridge; M_3, metal 3-fold hollow; M_4, metal 4-fold hollow; MP, metal−phosphorus bridge; P_1, phosphorus atop.

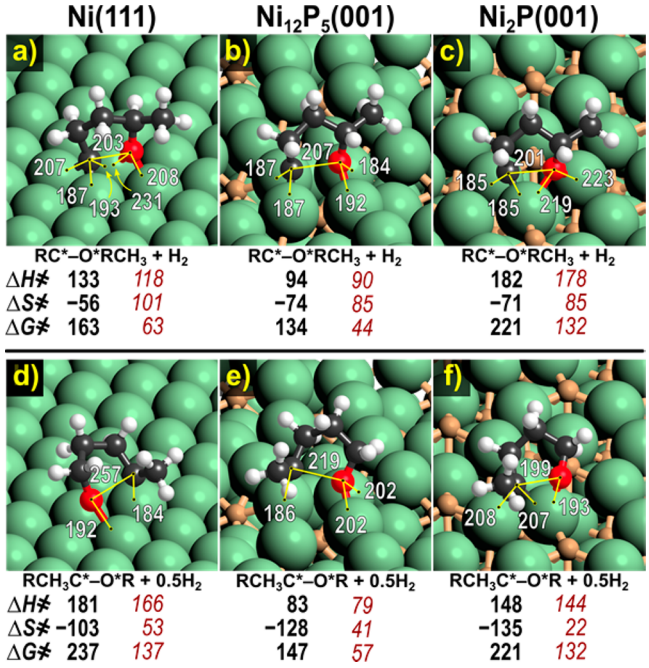

Figure 9. Transition-state structures for ^{2}C−O (a−c) and ^{3}C−O (d−f) on Ni, $Ni_{12}P_5$, and Ni_2P. Shown beneath each image are $\Delta H^{\ddagger}$ (kJ mol^{-1}), $\Delta S^{\ddagger}$ (J mol^{-1} K^{-1}), and $\Delta G^{\ddagger}$ (kJ mol^{-1}) for forming each state from a bare surface (black, bold) and from $C_5H_{10}O^*$-covered surface (red, italic). Important bond distances are shown in pm. Structures for other transition states are shown in the Supporting Information (Figure S11).

DOI: 10.1021/acscatal.7b04403
ACS Catal. 2018, 8, 7141−7157

interactions. Incorporating these interactions through empirical descriptions (DFT-D3) or by using exchange-correlation functionals that explicitly include van der Waals terms (e.g., optB88-vdW, optB86b-vdW, and vdW-DF2) increase Q_{MTHF} on Ni, $Ni_{12}P_5$, and Ni_2P surfaces by more than 30 kJ mol^{-1} (Table S3). Employing vdW-based methods may more accurately predict MTHF adsorption (i.e., positive heats of adsorption) while simultaneously overpredicting binding energies for chemisorbed species such as H* and CO*.[46] Dispersive forces are not included in calculations for energy and enthalpy barriers of elementary steps discussed in section 2.3, because they overpredict binding energies for chemisorbed species. Comparisons between enthalpy and energy barriers for elementary steps in the absence of dispersive forces are still relevant, while the absolute values have an offset from underestimated binding energy of MTHF.

Direct observation of adsorbates provides additional information about the chemical nature (i.e., metallic and acidic) of the catalyst surface. Measured vibrational frequencies for adsorbed CO (Figure S7) show a red shift in ν(CO) from 2142 cm^{-1} in the gas phase to 2035 cm^{-1} on 10 nm $Ni_{12}P_5$ and 2025, 1909, 1833, and 1710 cm^{-1} on 4 nm Ni, which reflects electron back-donation that weakens the C−O bond. The red shift in ν(CO) over Ni is more significant than that for $Ni_{12}P_5$ and is consistent with previous spectroscopic studies of adsorbed CO on Ni, $Ni_{12}P_5$, and Ni_2P surfaces,[47] which suggests a lesser extent of electron back-donation into the C−O bond on $Ni_{12}P_5$ and Ni_2P relative to Ni. Previous DFT calculations indicate a small transfer of charge from Ni to P (0.06 e^-) in Ni_2P,[48] producing Lewis acid sites (i.e., $Ni^{\delta+}$) that decrease the extent of electron back-donation from Ni atoms to the C−O bond relative to the Ni atoms in Ni nanoparticles while still retaining the metallic properties demonstrated by adsorbed CO.

Prior publications have implicated Brønsted[16,18,19,31,49] or Lewis[12,16,19,49] acid sites formed upon introduction of P atoms in reactions that cleave C−O bonds within oxygenates in the presence of H_2, yet it is not clear that these sites activate C−O bond rupture. In situ FTIR spectra obtained while cofeeding pyridine (C_5H_5N) with MTHF and H_2 (Figure S15; 1 kPa C_5H_5N, 5 kPa MTHF, 80 kPa H_2, 15 kPa He, 543 K) show different ring-breathing modes in adsorbed C_5H_5N (ν(CCN), modes 8a,[50,51] 8b,[50,51] and 19b[50,51]). The presence of mode 19b at 1445 cm^{-1} indicates the presence of Lewis acid sites[50,51] (i.e., $Ni^{\delta+}$) on all $Ni_{12}P_5$ and Ni_2P nanoparticles, while the feature at 1541 cm^{-1} that indicates Brønsted acid sites[50,51] is only present on 12 nm Ni_2P. Features of adsorbed C_5H_5N are not significant on the Ni catalyst. Although Brønsted acid sites are present on the 12 nm Ni_2P catalyst, Lewis acid sites outnumber Brønsted acid sites by a factor of ∼3 based on the ratio of peak areas and extinction coefficients of the bands at 1445 and 1541 cm^{-1}.[52] Brønsted acid sites likely form by incomplete reduction of the phosphide precursor forming P−OH groups.[16] Pentane forms with significantly higher selectivity over 12 nm Ni_2P nanoparticles (80 C-%) compared with the Ni and $Ni_{12}P_5$ nanoparticles (0−3 and 3−10 C-%, respectively), which could indicate that the Brønsted acid sites facilitate full deoxygenation similar to previous works studying the deoxygenation of saturated furanic compounds (e.g., THF,[53] MTHF[54]) to aliphatic dienes over solid acid catalysts (e.g., SiO_2−Al_2O_3,[54] H-ZSM-5,[54] P−Al−BEA,[53] and phosphorus self-pillared pentasil[53]). Kumbhalkar et al. note that the formation rate of pentadiene from MTHF is proportional to the concentration of Brønsted acid sites.[54] Additionally, pentane formation rates ($r_{pentane}$) show a much weaker inverse dependence in [H_2] (Figure S16a, $r_{pentane} \sim [H_2]^{-0.16}$) than either C−O bond rupture pathway over 12 nm Ni_2P. The significant difference of $r_{pentane}$ dependence on [H_2] and activation enthalpies (Figure S16b) compared with r_{2C-O} and r_{3C-O} combined with the coexistence of high selectivity toward pentane and the presence of Brønsted acid sites on 12 nm Ni_2P strongly suggests that a separate C−O bond rupture pathway occurs over the Brønsted acid sites to form significant amounts of pentane, while the other C−O bond rupture products (e.g., 2-pentanone, 2-pentanol, butane) form over the Ni_2P surface. While spectra of adsorbed CO and C_5H_5N under reaction conditions show the presence of metallic and Lewis acidic sites on all $Ni_{12}P_5$ and Ni_2P surfaces, these spectra do not indicate if they exist in the same location and do not link chemical properties to the active sites for C−O bond rupture.

Figure 10 shows that both r_{2C-O} and r_{3C-O} decrease in proportion to NH_3 pressure ([NH_3]; $r_{C-O} \sim [NH_3]^{-1}$) when

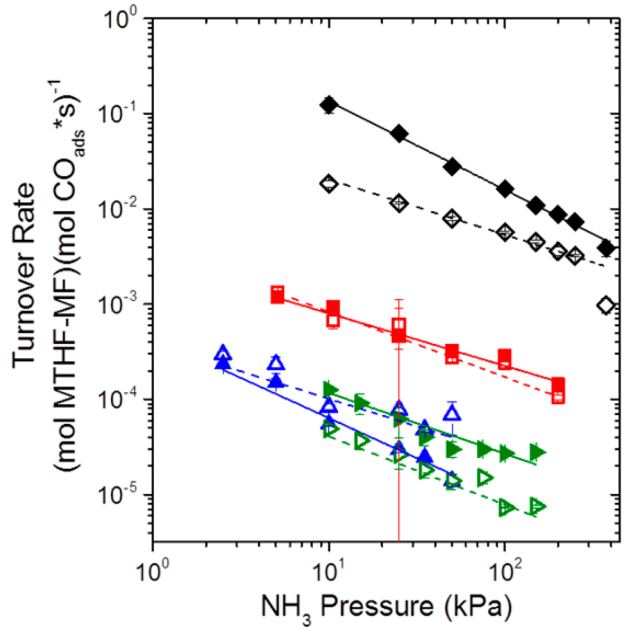

Figure 10. Change in consumption of the MTHF-MF reactant pool to form pentanal and subsequent ^{3}C−O bond rupture products (open symbols) and 2-penten-4-one and subsequent ^{2}C−O bond rupture products (solid symbols) indicated in Scheme 1 with NH_3 pressure over SiO_2-supported 4 nm Ni (black diamonds), 5 nm $Ni_{12}P_5$ (green triangles), 19 nm $Ni_{12}P_5$ (red squares), and 12 nm Ni_2P (blue triangles) in 0.25 MPa H_2 and 5 kPa MTHF at 543 K. Trend lines indicate power law fits. Figure S17 displays these data as total turnover rates and selectivities.

NH_3 is introduced with the reactants (5−350 kPa NH_3, 5 kPa MTHF, 0.25 MPa H_2, 543 K), which indicates that the ensemble of Ni atoms that facilitate C−O bond rupture on $Ni_{12}P_5$ and Ni_2P can be occupied and inhibited by the adsorption of a single NH_3 molecule at the atop position of one Ni atom (M_1) within the active ensemble (M_3 or M_{4a}) on Ni_2P and $Ni_{12}P_5$ surfaces, respectively (Table S2). Site requirements for all adsorbates (H*, CO*, NH_3*, and $C_5H_{10}O$*) are identical between each C−O bond rupture pathway on $Ni_{12}P_5$ and Ni_2P, which is consistent with the assumption that C−O bond rupture occurs through a single-

DOI: 10.1021/acscatal.7b04403
ACS Catal. 2018, 8, 7141−7157

Table 1. Measured and Predicted Activation Enthalpies (kJ mol^{-1}) for ^{2}C−O and ^{3}C−O Bond Rupture Pathways on $C_5H_{10}O$*-Covered Ni, $Ni_{12}P_5$, and Ni_2P Surfaces ($\Delta H_{C5H10O*}^{\ddagger}$) and Their Differences ($\Delta\Delta H_{2C-3C}^{\ddagger}$)

	$C_5H_{10}O^*$ ($\Delta H_{C5H10O*}^{\ddagger}$)					
	measured[a]		predicted[b]		$\Delta\Delta H_{2C-3C}^{\ddagger}$	
catalyst	^{2}C−O	^{3}C−O	^{2}C−O	^{3}C−O	measured	predicted
12 nm Ni_2P[c]	193 ± 9	170 ± 9	178	144	23 ± 12	34
19 nm $Ni_{12}P_5$[d]	180 ± 5	155 ± 5	90	79	25 ± 7	11
5 nm $Ni_{12}P_5$[d]	144 ± 12	134 ± 12	90	79	10 ± 16	11
4 nm Ni[d]	119 ± 8	130 ± 4	118	166	−11 ± 8	−48

[a]Measured values extracted from Figures 11 and S18. [b]Predicted values over Ni(111), $Ni_{12}P_5$(001), and Ni_2P(001) at 543 K. [c]Measured at 0.125 MPa H_2. [d]Measured at 1 MPa H_2

site mechanism as described by eqs 6a and 6b. NH_3 also inhibits C−O bond rupture rates proportionally over Ni nanoparticles, which do not have Lewis or Brønsted acid sites present based on in situ measurements with pyridine (Figure S15); therefore, the spectroscopic and kinetic evidence alone cannot show that the active site for C−O bond rupture on $Ni_{12}P_5$ and Ni_2P is acidic. Differences in selectivity during C−O bond rupture reactions have previously been attributed to adjustments in acid site concentration by manipulating metal to phosphorus ratio[18] or operating in the presence of mineral[55] or solid[56,57] acids. Here, measured values for χ are independent of [NH_3] on Ni, $Ni_{12}P_5$, and Ni_2P catalysts, which indicates that the addition of P atoms adjusts the electronic structure of the Ni atoms rather than creating a second type of active site. A single active site for both C−O bond rupture pathways is consistent with predicted transition states for ^{m}C−O bond rupture, H*, CO*, and NH_3* all exclusively bound to Ni atoms instead of P atoms (Figure 9 and Table S3). The following section uses quantitative comparisons of measured activation enthalpies under different surface coverages and DFT-derived activation barriers to infer mechanistic details of C−O bond rupture pathways in MTHF.

2.5. Comparisons of Activation Enthalpies for C−O Bond Rupture on Ni, $Ni_{12}P_5$, and Ni_2P Nanoparticles with Different Surface Coverages. Experimental and computational results show agreement for the proposed mechanism for ^{m}C−O bond rupture within MTHF over Ni, $Ni_{12}P_5$, and Ni_2P nanoparticles at active sites comprised of Ni ensembles; however, the trends in selectivities and active site properties can be understood in greater detail by analysis of the changes to measured activation enthalpies that result from differences in the MASI present during catalysis. Kinetic measurements indicate that elementary steps leading to C−O bond rupture (Scheme 2, 2.1−2.3a and 2.1−2.2b) are quasi-equilibrated. Transition-state theory (TST) provides a hypothetical equilibrium between a transition-state complex and the preceding reactive intermediate (e.g., C_5H_8O* and $C_5H_8O^{*\ddagger}$). These combined equilibria can be expressed as

$$C_5H_{10}O + * \overset{K_{m_{C-O}}^{\ddagger}}{\longleftrightarrow} \left(2 - \frac{m}{2}\right)H_2 + {}^mC_5H_{6+m}O^{*\ddagger} \quad (7)$$

where $K_{m_{C-O}}^{\ddagger}$ is the equilibrium constant for forming the ^{m}C−O bond rupture transition state ($^mC_5H_{6+m}O^{*\ddagger}$) and a stoichiometric amount of gas-phase H_2 from MTHF and a bare surface. The full rate expression can be expressed in terms of the pressures of gas phase species and $K_{m_{C-O}}^{\ddagger}$ using the conventions of TST and the quasi-equilibrated nature of eq 7 to find

$$\frac{r_{m_{C-O}}}{[L]} = \frac{k_bT}{h}K_{m_{C-O}}^{\ddagger}[\text{MTHF}][H_2]^{-(2-m/2)} \quad (8)$$

Here h and k_b are the Planck and Boltzmann constants, respectively, and T is the temperature. Expanding $K_{m_{C-O}}^{\ddagger}$ to reflect the activation entropy ($\Delta S^{\ddagger}$) and enthalpy ($\Delta H^{\ddagger}$) of eq 8 results in the following equation

$$\frac{r_{m_{C-O}}}{[L]} = \frac{k_bT}{h}e^{\Delta S^{\ddagger}/R}e^{-\Delta H^{\ddagger}/RT}[\text{MTHF}][H_2]^{-(2-m/2)} \quad (9)$$

This expression describes reactions on a predominantly bare surface (i.e., * as MASI) but can be modified to describe reactions occurring on CO*-, H*-, or $C_5H_{10}O$*-covered surfaces as shown in the Supporting Information (Section S2).

Table 1 displays both the experimental and the computational results for $\Delta H^{\ddagger}$ from a $C_5H_{10}O$*-covered surface. Experimental values for $K_{m_{C-O}}^{\ddagger}$ and subsequently $\Delta H^{\ddagger}$ are determined from measured turnover rates for ^{3}C−O and ^{2}C−O bond rupture as functions of inverse temperature over Ni, $Ni_{12}P_5$, and Ni_2P nanoparticles (Figures 11 and S18, 5 kPa MTHF, 0.125−1 MPa H_2, 473−583 K).

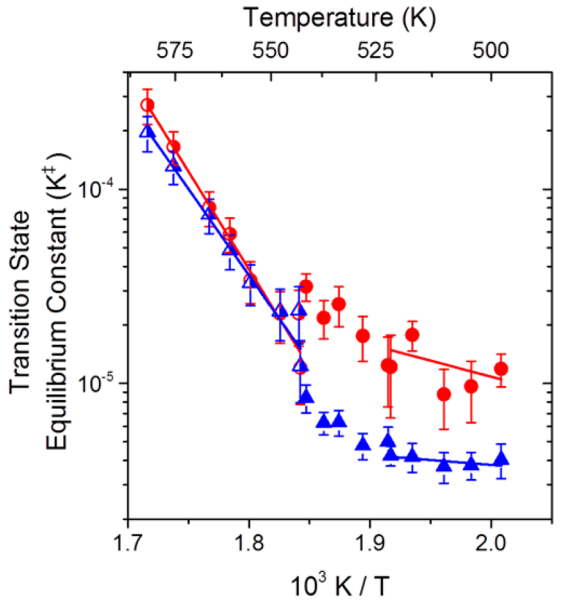

Figure 11. Transition-state equilibrium constants ($K^{\ddagger}$) for ^{2}C−O (red circles) and ^{3}C−O (blue triangles) bond rupture pathways as a function of inverse temperature on silica-supported 12 nm Ni_2P (5 kPa MTHF, half filled, 0.125 MPa H_2; filled, 1 MPa H_2).

DOI: 10.1021/acscatal.7b04403
ACS Catal. 2018, 8, 7141−7157

Rates measured across the Ni, $Ni_{12}P_5$, and Ni_2P nanoparticles at the same conditions (e.g., Figure 5, 1 MPa H_2, 5 kPa MTHF, and 543 K) indicate that the turnover rates for C−O bond rupture over $Ni_{12}P_5$ are greater than those over Ni_2P; however, the reaction conditions (e.g., T, [CO]) strongly influence relative rates. Comparisons with previous studies that show greater turnover frequencies occur over the more metal-rich phases of phosphides including C−O bond rupture of guaiacol over $Ni_{12}P_5$ compared to Ni_2P at differential conversion[18] and furan over SiO_2-supported Ru_2P and RuP,[12] but direct comparison of materials needs to account for all reaction conditions. The decrease in C−O bond rupture rates with increasing P:Ni ratio under conditions with a $C_5H_{10}O^*$ surface (Figure 5, 1 MPa H_2, 5 kPa MTHF, and 543 K) is also consistent with the increase in measured $\Delta H^{\ddagger}$ with increasing P:Ni on $C_5H_{10}O^*$ surfaces and greater predicted $\Delta H^{\ddagger}$ over $Ni_2P(001)$ compared with $Ni_{12}P_5(001)$ (Table 1). While absolute values for $\Delta H^{\ddagger}$ deviate between experimental and computational results, the difference in activation enthalpies between the ^{2}C−O and the ^{3}C−O bond rupture pathways ($\Delta\Delta H_{2C-3C}^{\ddagger}$) is consistent for the $Ni_{12}P_5$ and Ni_2P materials (Table 1). Positive values for $\Delta\Delta H_{2C-3C}^{\ddagger}$ indicate ^{3}C−O bond rupture is more enthalpically favorable over ^{2}C−O bond rupture, and $\Delta\Delta H_{2C-3C}^{\ddagger}$ increases with P:Ni ratio, similar to χ (Figure 2). These systematic increases in $\Delta\Delta H_{2C-3C}^{\ddagger}$ and χ values with the P:Ni ratio may result from differences in binding modes and orientation of intermediates over Ni, $Ni_{12}P_5$, and Ni_2P surfaces, as suggested by the predicted transition-state structures (Figure 9). We are currently conducting in situ infrared spectroscopy to determine the differences between the binding modes of MTHF-derived adsorbates on Ni, $Ni_{12}P_5$, and Ni_2P surfaces.

Previous studies on transition metal surfaces show that trends in the binding energies of hydrocarbons, alcohols, thiols, and amino acids can be related to the adsorption energies of chemisorbed fragments such as CH_x^*, OH_x^*, SH_x^*, and NH_x^*.[58−61] As shown in Figure 9, C−O bond cleavage transition states interact with the catalyst surfaces through the C and O atoms of the cleaved bond. These transition states can be represented by a simpler model, in which the C and O atoms are constrained to their transition-state positions and all substituents bound to these C and O atoms are replaced with H atoms (i.e., coadsorbed CH* and OH* replace the ^{2}C−O‡ and coadsorbed CH_2^* and OH* replace the ^{3}C−O‡). Alternatively, the pair of fragments that represents each transition state can be relaxed and their enthalpies calculated at their most stable binding sites. Figure 12 shows that either method for calculation provides differences in adsorption enthalpies between coadsorbed CH* and OH* and coadsorbed CH_2^* and OH* ($\Delta\Delta H_{2C-3C}$) that are negative for Ni (indicating favorable ^{2}C−O bond cleavage) and positive for $Ni_{12}P_5$ and Ni_2P (indicating favorable ^{3}C−O bond cleavage). Qualitatively, these comparisons of these values for simple analogues for the more complex C−O bond cleavage transition states show that calculations for the stable binding modes of CH_x^* and OH* can provide estimates for the values of $\Delta\Delta H_{2C-3C}^{\ddagger}$ that capture the preference for a given metal or metal phosphide to cleave hindered or unhindered C−O bonds in MTHF (and likely other oxygenates) shown in the full transition-state models (Figure 12). Therefore, the binding energies of simple adsorbates (CH_x^* and OH*) can be calculated to rapidly screen C−O cleavage selectivity on complex catalytic surfaces (such as

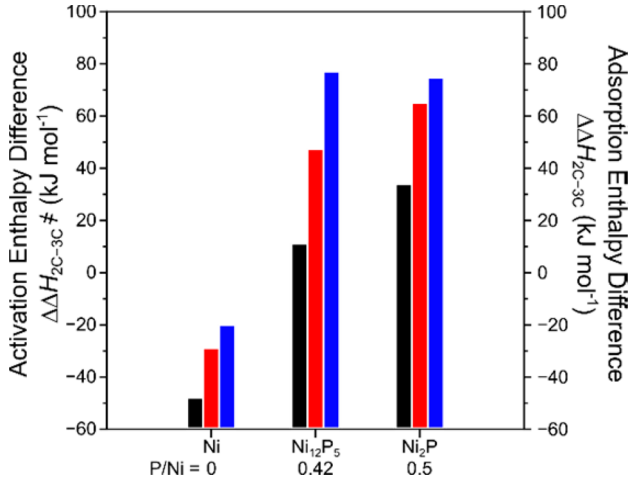

Figure 12. DFT-predicted differences in activation enthalpies ($\Delta\Delta H_{2C-3C}^{\ddagger}$) (black) and differences in adsorption enthalpies for CH_x^* and OH* coadsorbed in binding modes that match the transition state (red) and CH_x^* and OH* coadsorbed in their most stable binding sites (blue) (x = 1 for ^{2}C and 2 for ^{3}C).

MPs). However, a more thorough DFT analysis (e.g., those data shown in Figures 6, 7, S12, and S14) is needed to verify the reversibility and kinetic relevance of C−H and C−O bond rupture events and to provide more accurate predictions for C−O bond rupture selectivities.

Figure 13 shows measured values of χ as a function of [H_2] on Ni, $Ni_{12}P_5$, and Ni_2P nanoparticles as well as predicted χ

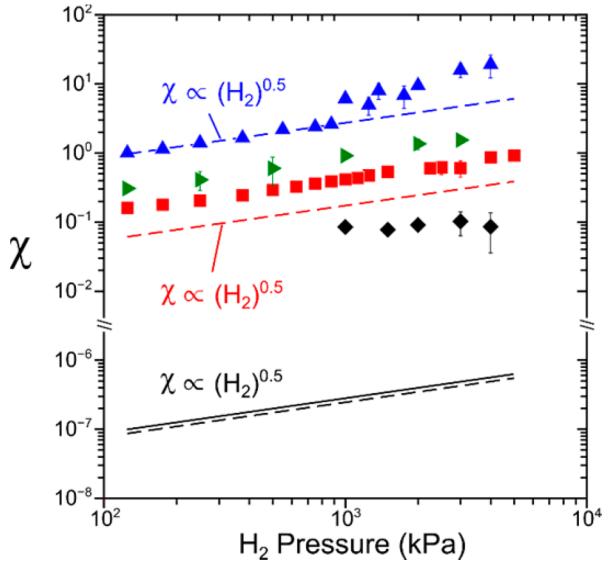

Figure 13. DFT-predicted ratios of ^{3}C−O to ^{2}C−O bond rupture rates (χ) on Ni(111) (black dashed line), Ni(100) (black solid line), $Ni_{12}P_5(001)$ (red dashed line), and $Ni_2P(001)$ (blue dashed line) surfaces, and measured values of χ as a function of H_2 pressure for 4 nm Ni (black solid diamonds), 12 nm Ni_2P (blue solid triangles), 5 nm $Ni_{12}P_5$ (green solid right-facing triangles), and 19 nm $Ni_{12}P_5$ (red solid squares) at 5 kPa MTHF and 543 K.

values calculated using eqs 1 and 9 with DFT-derived values of $\Delta H^{\ddagger}$ and $\Delta S^{\ddagger}$ for all ^{m}C−O cleavage transition states (Figure 9 and S11) on Ni(111), Ni(100), $Ni_{12}P_5(001)$, and $Ni_2P(001)$. Calculated $\Delta G^{\ddagger}$ values predict that ^{3}C−O selectivity (χ = 0.2, at 1 MPa H_2) is lower on M_{4a} sites of $Ni_{12}P_5(001)$ than on the

DOI: 10.1021/acscatal.7b04403
ACS Catal. 2018, 8, 7141−7157

$Ni_2P(001)$ surface, which agrees with differences in measured χ values in Figure 13. Predicted values of $\Delta\Delta H_{2C\text{-}3C}^{\ddagger}$ (Table 1) and χ (Figure 13) over Ni are significantly different from the measured values of each, which may result from C−O bond rupture occurring on sites other than the (111) or (100) surfaces (e.g., corner or edge sites). Overall, the trends in predicted C−O bond rupture selectivities are consistent with the trends in measured values of χ (Figure 13) and measured $\Delta\Delta H_{2C\text{-}3C}^{\ddagger}$ (Table 1): the selectivity toward ^{3}C−O bond rupture increases with increased ratios of P:Ni.

Measured $\Delta H^{\ddagger}$ values that differ between lower and higher reaction temperatures (Figure 11) reflect differences between the MASI that exist under these conditions. The value of $\Delta H^{\ddagger}$ increases from 23 to 193 kJ mol^{-1} for ^{2}C−O bond rupture and from 18 to 170 kJ mol^{-1} for ^{3}C−O bond rupture over 12 nm Ni_2P (Figure 11 and Table S4) as the temperature increases above 543 K and the $[H_2]$ decreases from 1 to 0.125 MPa. This increase in $\Delta H^{\ddagger}$ values combined with changes in the dependence of rates on $[H_2]$ suggests that the MASI changes from H* to $C_5H_{10}O$*. The increase in $\Delta H^{\ddagger}$ is consistent also with values for Q_{MTHF} that are predicted to be greater than that of Q_{H2} over $Ni_2P(001)$ when dispersion forces are included (Table S3). Upon introducing CO (5 kPa) with the reactants over $Ni_{12}P_5$ and Ni nanoparticles (Figure S18), values for $\Delta H^{\ddagger}$ for both C−O bond rupture pathways increase as the result of a change from $C_5H_{10}O$* to CO* as the MASI. The changes in $\Delta H^{\ddagger}$ with temperature and rate dependence with $[H_2]$ and [MTHF] over Ni, $Ni_{12}P_5$, and Ni_2P nanoparticles occur at the same temperature or pressures for both C−O bond rupture pathways, which suggests adsorbates (H*, $C_5H_{10}O$*, and CO*) possess the same binding energy for both ^{2}C−O and ^{3}C−O bond rupture active sites. Collectively, these observations suggest that the same site catalyzes both C−O bond rupture pathways on each of these catalysts.

Differences in $\Delta H^{\ddagger}$ values that result from differences in MASIs should be equivalent for ^{2}C−O and ^{3}C−O bond rupture if a single site catalyzes both pathways as demonstrated by 12 nm Ni_2P and 4 nm Ni (Table S5). Neither 5 nor 19 nm $Ni_{12}P_5$ nanoparticles show equivalent changes in $\Delta H^{\ddagger}$ for ^{2}C−O and ^{3}C−O bond rupture as the MASI transitions from $C_5H_{10}O$* to CO*. This may reflect a difference between the interactions between CO* and the ^{2}C−O and ^{3}C−O transition states, as demonstrated for CO hydrogenation over Ru;[62] however, additional studies over $Ni_{12}P_5$ and Ni_2P nanoparticles with narrower size distributions need to confirm this hypothesis. While $Ni_{12}P_5$ nanoparticles do not show equivalent changes in $\Delta H^{\ddagger}$ values between ^{2}C−O and ^{3}C−O bond rupture with the MASI transitions, the consistency between measured and predicted transition-state composition, C−O bond rupture mechanism, active site chemical nature, and selectivity provides strong evidence that the same ensembles of Ni atoms catalyze both ^{2}C−O and ^{3}C−O bond rupture on Ni, $Ni_{12}P_5$, and Ni_2P catalysts.

3. CONCLUSIONS

Turnover rates for the hydrogenolysis of ^{2}C−O and ^{3}C−O bonds within MTHF were measured as a function of MTHF, H_2, and CO pressure over SiO_2-supported Ni, $Ni_{12}P_5$, and Ni_2P catalysts. These kinetic data were combined with DFT calculations on the low-energy surfaces of these catalysts to determine the reaction mechanism and the nature of the active sites for C−O bond cleavage on metal phosphide catalysts. H_2 pressure inhibits ^{3}C−O and ^{2}C−O bond cleavage rates to different extents, and the degree of H_2 inhibition suggests that the transition states for these pathways have lost 1 or 2 H atoms from gas-phase MTHF, respectively. Consequentially, the ratio of ^{3}C−O to ^{2}C−O bond rupture rates increases with H_2 pressure across Ni, $Ni_{12}P_5$, and Ni_2P catalysts. Predicted enthalpy barriers for C−O and C−H bond rupture within MTHF intermediates over Ni, $Ni_{12}P_5$, and Ni_2P surfaces indicate ^{m}C−H bond rupture is at least ∼30 kJ mol^{-1} more favorable than ^{m}C−O bond rupture until the ^{m}C is fully dehydrogenated. Thus, MTHF undergoes quasi-equilibrated dehydrogenation steps that remove all hydrogen atoms from ^{m}C before the kinetically relevant ^{m}C−O bond rupture, which is consistent with quasi-equilibrium between MTHF, MF, and H_2 as well as the measured effect of H_2 pressure on rates.

Site requirements are identical for ^{3}C−O and ^{2}C−O bond rupture across Ni, $Ni_{12}P_5$, and Ni_2P catalysts as shown by constant C−O cleavage ratios over wide ranges of the pressures for CO, NH_3, and MTHF. Comparisons of predicted adsorption energies for intermediates and measured differences in activation enthalpies of H-, CO-, and $C_5H_{10}O$-covered surfaces indicate both C−O bond rupture pathways are catalyzed by ensembles of 3−4 Ni atoms on Ni, $Ni_{12}P_5$, and Ni_2P catalysts. This conclusion indicates that Brønsted acid sites formed by the incomplete reduction of P−OH groups are not catalytically relevant for the elementary steps described here. Measured and predicted activation enthalpies are lower for ^{3}C−O bond rupture relative to ^{2}C−O bond rupture (by 10−34 kJ mol^{-1}) over $Ni_{12}P_5$ and Ni_2P surfaces, which is consistent with the observation that the preference to selectively cleave ^{3}C−O bonds over ^{2}C−O bonds increases along with the P:Ni ratio of the catalyst. DFT predictions for Ni-terminated $Ni_{12}P_5(001)$ and $Ni_2P(001)$ surfaces reproduce these selectivity patterns, whereas P-terminated structures do not, which further indicates that ensembles of Ni atoms exposed on supported $Ni_{12}P_5$ and Ni_2P nanoparticles are the active sites and surfaces. Furthermore, DFT calculations of CH_x* and OH* adsorption energies qualitatively predict C−O bond rupture selectivities on Ni, $Ni_{12}P_5$, and Ni_2P catalyst surfaces and suggest strategies for the rapid evaluation of complex catalysts for selective C−O cleavage.

The proposed mechanism, active site characteristics, and calculated energy and enthalpy barriers demonstrate that the temperature, H_2 pressure, and P:Ni ratio of the catalyst ultimately control the turnover rates and selectivity between C−O bond rupture within oxygenates. Ni_2P nanoparticles show greater resistance to CO poisoning than do Ni and $Ni_{12}P_5$ nanoparticles no matter whether the CO comes from the decarbonylation of aldehydes or is intentionally introduced. Ni_2P catalysts also form significantly more fully deoxygenated products, which may be less desirable depending on the intended application of the product stream as fuels or high-value chemicals. Future studies inspecting the implementation of $Ni_{12}P_5$ and Ni_2P catalysts for selective hydrogenolysis of oxygenates will need to balance the decrease in C−O bond rupture rates and increase in selectivity toward hindered C−O bond rupture with increasing P:Ni ratio while also considering additional functional groups present within bio-oil.

4. MATERIALS, METHODS, AND CHARACTERIZATION

4.1. Synthesis and Characterization of Supported Nickel and Nickel Phosphide Catalysts. *4.1.1. Synthesis of Silica Supported Nickel and Nickel Phosphide Nanoparticles.* Nickel phosphide catalysts supported on high surface

DOI: 10.1021/acscatal.7b04403
ACS Catal. 2018, 8, 7141−7157

Table 2. Catalyst Composition and Nanoparticle Dispersion

		composition[b]		CO uptake[c]		
catalyst	$\langle d_{TEM}\rangle$[a] (nm)	mol % Ni	mol % P	mmol CO_{ads}/mol Ni	μmol CO_{ads}/g_{cat}	Ni dispersion[d] (%)
Ni_2P	12 ± 3	1.94	1.94	24	8	7.3
$Ni_{12}P_5$	19 ± 7	2.03	0.58	10	3.5	4.1
$Ni_{12}P_5$	10 ± 3	1.95	0.58			
$Ni_{12}P_5$	5 ± 1	1.67	0.58	111	31	44.6
Ni	4 ± 1	1.96	0	25	8.1	7.4

[a]Surface area normalized average nanoparticle diameter determined from >300 nanoparticles. [b]Elemental composition of samples determined by inductively coupled plasma optical emission spectroscopy (ICP-OES) following digestion in strong acid solutions. [c]CO uptake determined by adsorption isotherms at 298 K following a reductive treatment in 50 cm^3 min^{-1} H_2 at 673 K for 1 h and subsequent vacuum annealing at 673 K for 1 h. [d]Ni dispersion calculated from CO uptake and the calculated preferred binding orientation for CO as 3- or 4-fold Ni hollows as described in the Supporting Information Table S3

area silica were prepared using strong electrostatic adsorption (SEA)[63] or incipient wetness impregnation (IWI) methods. The SEA method involved adding the nickel precursor $Ni(NO_3)_2{\cdot}(H_2O)_6$ to DI water followed by adding an NH_4OH aqueous solution to the precursor solution to form an aqueous $[Ni(NH_3)_6]^{2+}$ complex,[63] after which SiO_2 was added to the aqueous solution and stirred. The solids were then separated from the liquid by vacuum filtration and rinsed with DI water. Samples were prepared by IWI by creating an aqueous solution of the same nickel precursor and adding this solution dropwise to clean, dry SiO_2, achieving treated incipient wetness. Wet solids derived from both SEA and IWI were dried in stagnant air. Subsequently, the dried solids were then subjected to oxidative, reductive, and passivative heat treatments as detailed in the Supporting Information (Section S3.1).

A sample of the Ni−SiO_2 was set aside (1.9 wt %), while the remaining Ni−SiO_2 was impregnated with a phosphorous acid solution to achieve molar Ni:P ratios of 2:1 and 1:1. These samples were dried and then treated with oxidative, reductive, and passivative heat treatments.

4.1.2. Metal Phosphide Nanoparticle Sizes and Composition. The crystallographic structures of $Ni_{12}P_5$−SiO_2 and Ni_2P-SiO_2 materials were determined using powder X-ray diffraction (XRD) (Figure S19). High weight loading catalysts (18 wt %) were used to obtain observable diffraction patterns, and these agree closely with published results for $Ni_{12}P_5$ and Ni_2P powders.[18] Nanoparticle diameters were measured using transmission electron microscopy (TEM). The diameters of more than 300 particles were counted from the TEM images obtained to calculate surface area normalized average nanoparticle diameters ($\langle d_{TEM}\rangle$, Table 2) for each sample. Sample images and nanoparticle size distributions for each catalyst are shown in the Supporting Information (Figures S20−S24). Chemisorbed CO was used to measure the number of exposed surface sites per mole of Ni atoms assuming a Ni ensemble site. Total uptake of CO for all materials is shown in Table 2, and adsorption isotherms for each sample are shown in the SI (Figure S25).

4.1.3. Temperature-Programmed Reduction of Catalysts. Temperature-programmed reduction (TPR) was performed on dried Ni, $Ni_{12}P_5$, and Ni_2P samples in order to confirm that the Ni, $Ni_{12}P_5$, and Ni_2P materials were reduced by the thermal treatments in H_2/He mixtures. Prior to TPR experiments, the samples were heated to 773 K and held for 6 h in flowing dry air with the intent to fully oxidize the samples. Samples were then cooled to 303 K, after which the sample was heated to 1073 at 0.05 K s^{-1} while the H_2 consumption and H_2O production were monitored using a quadrupole mass spectrometer as a function of sample temperature using the QMS. Figure S26 shows reduction profiles indicating the formation of a nickel phosphide phase as opposed to separate nickel and phosphide phases, because the $Ni_{12}P_5$ and Ni_2P reduction profiles are not a linear combination of the $Ni(NO_3)_2$ and H_3PO_3 reduction profiles, rather the presence of Ni decreases the reduction temperature of the phosphite group.

4.1.4. In Situ Fourier Transform Infrared Spectroscopy. Reactive intermediates and basic probe molecules (i.e., pyridine) formed or adsorbed during hydrogenolysis of 2-methyltetrahydrofuran (MTHF) over self-supporting pellets of Ni, $Ni_{12}P_5$, and Ni_2P catalysts were observed using in situ transmission Fourier transform infrared (FTIR) spectroscopy using a custom-made transmission cell as previously described.[64] Liquid reactants (MTHF and pyridine) were introduced using a syringe pump in a crossflow configuration with the primary gas flow (H_2 and He) controlled by mass flow controllers. Prior to acquiring spectra, the catalyst was pretreated in situ to 673 K in flowing H_2 at ambient pressure. Steady state measurements were obtained while flowing MTHF, H_2, and He prior to introducing pyridine. The subsequent spectra analysis (e.g., subtraction of the gas-phase contribution, baseline correction, and data smoothing) was performed using OriginLab's OriginPro software, as detailed in the Supporting Information Section S3.1.5.

4.2. Catalytic Rate Measurements. Rate and selectivity measurements were conducted in a packed bed reactor heated with a three-zone electrically heated furnace and pressurized (0.1−6.0 MPa) using a dome-loaded back-pressure regulator, which was controlled by an electronic pressure regulator. The reactor pressure was monitored upstream and downstream of the catalyst bed. Comparisons of these measurements showed that the pressure drop across the catalyst bed was less than 1% of the total pressure. Gas flow rates (H_2, CO, and NH_3) were controlled using mass flow controllers. The flow rates of liquids including MTHF and 2-methylfuran (MF) were controlled using a stainless steel syringe pump. All transfer lines downstream of the liquid inlet were heated to avoid condensation of the products or reactant.

Catalysts were pretreated in situ by heating to 673 K flowing H_2 prior to all catalytic measurements. The effluent of the reactor was characterized using online gas chromatography equipped with a flame ionization detector and thermal conductivity detector. A complete list of these standards and calculations for sensitivity factors is shown in the Supporting Information (Section S3). Conversions were calculated on a

DOI: 10.1021/acscatal.7b04403
ACS Catal. 2018, 8, 7141−7157

carbon basis based on the amount of carbon that appears in the products. The carbon and oxygen balance closes within ±10%. Turnover rates are normalized by the number of CO adsorption sites determined through chemisorption experiments described in section 4.1.2. Data reported as a function of conversion, reactant pressure, and temperature follow an initial break-in period (Figure S27), and turnover rates are corrected for the number of active sites lost over time, as described in the Supporting Information (Section S3.2.1).

4.3. Computational Methods. *4.3.1. Nickel and Nickel Phosphide Lattice Parameters and Surface Formation Energies.* Periodic plane-wave density functional theory (DFT) calculations were performed using the Vienna ab initio simulation package (VASP).[65−68] Plane waves were constructed using projector augmented-wave (PAW) potentials with an energy cutoff of 396 eV.[69,70] The Perdew−Burke−Ernzerhof (PBE) form of the generalized gradient approximation (GGA) was used to determine exchange and correlation energies for bulk and surface formation calculations, which should give a more accurate estimation of lattice parameters.[71−73] Wave functions were converged to within 10^{-8} eV, and forces were computed using a fast Fourier transform (FFT) grid; the maximum force on each atom was converged to <0.01 eV $Å^{-1}$. The unit cells of bulk Ni (space group $Fm\bar{3}m$),[74] Ni_2P (space group $P\bar{6}2m$),[75] and $Ni_{12}P_5$ (space group $I4/m$)[75] were built based on crystallographic data, and the lattice parameters were then optimized using DFT. The optimized bulk lattice parameters for Ni ($a = b = c =$ 3.52 Å), Ni_2P ($a = b =$ 5.87 Å and $c =$ 3.37 Å) and $Ni_{12}P_5$ ($a = b =$ 8.63 Å, $c =$ 5.07 Å) were consistent with previous DFT studies[76] and in close agreement with the measured values $a = b = c =$ 3.52 Å,[74] $a = b =$ 5.86 Å and $c =$ 3.38 Å,[77] and $a = b =$ 8.65 Å, and $c =$ 5.07 Å.[77] Further details of the bulk calculations are presented in the Supporting Information (Section S3.3). All Ni calculations were run spin polarized because of its ferromagnetic properties. Calculations showed less than 10^{-4} eV energy difference between spin- and nonspin-polarized calculations for $Ni_{12}P_5(001)$ and $Ni_2P(001)$ calculations, consistent with previous DFT studies,[76] so all calculations of $Ni_{12}P_5(001)$ and $Ni_2P(001)$ surfaces were done without spin polarization.

The closed-packed Ni(111) surface has the lowest surface formation energy (1008 kJ mol^{-1} nm^{-2}) compared to Ni(100) (1142 kJ mol^{-1} nm^{-2}) and Ni(110) (1211 kJ mol^{-1} nm^{-2}), as well established for transition metals.[78] For Ni_2P and $N_{12}P_5$ surfaces, there is an alternation of planes in the z direction that have different Ni and P composition; scanning tunneling microscope (STM) images confirm the existence of two different terminations on $Ni_2P(001)$ single crystals.[79] Our DFT calculations indicate that the Ni-rich terminations in $Ni_2P(001)$ and $Ni_{12}P_5(001)$ have the lowest surface formation energies (823 kJ mol^{-1} nm^{-2} and 963 kJ mol^{-1} nm^{-2}, respectively) (Figure S29). Thus, the Ni(111), $Ni_{12}P_5(001)$, and $Ni_2P(001)$ surfaces were used, although the kinetic relevance of other surfaces cannot be eliminated. These surfaces were modeled with k-point meshes[80] of 4 × 4 × 1 and 5 × 5 × 1 for Ni(111), $Ni_{12}P_5(001)$, and $Ni_2P(001)$ surfaces, and the energies changed by less than 1×10^{-2} eV if larger k-point meshes were used, as further detailed in the SI (Section S3.3.2, Figures S28−30).

4.3.2. Energy Barrier Calculations. The revised Perdew−Burke−Ernzerhof (RPBE) functional was used for calculations of adsorption, reaction, and activation energies because it exhibits better performance in predicting adsorption energies in metal surfaces.[71−73] Additional calculations (discussed in sections 2.3 and 2.4) were performed using optB88-vdW,[81] optB86b-vdW,[82] RPBE-D3BJ,[83] and vdW-DF2[84] functionals which attempt to include dispersion interactions such as van der Waals forces. Wave functions were converged to within 10^{-6} eV, and structures were relaxed until all forces on unconstrained atoms were <0.05 eV$Å^{-1}$. Gaseous species were modeled within 16 × 16 × 16 Å unit cells of vacuum. The Ni(111) catalyst surface was modeled as a 3 × 3 closed-packed periodic lattice with four layers in the orthogonal direction and a 10 Å vacuum between slabs; the bottom two layers were fixed in their bulk positions and the top two layers relaxed. After geometric convergence, a single-point calculation with a (8 × 8 × 1) k-point mesh was performed to determine the electronic energy. The $Ni_2P(001)$ and $Ni_{12}P_5(001)$ surfaces shown in Figures 8 and S31 were modeled with two repeating units and a 10 Å vacuum in the z direction. The bottom repeat units (two atomic layers for Ni_2P and four atomic layers for $Ni_{12}P_5$, Figure S31b and S31c) were fixed in their bulk positions, while all other atoms were relaxed.

Transition-state structures were obtained for each elementary reaction by using the nudged elastic band (NEB) method[85,86] and the dimer method.[87] The NEB method was carried out using 16 images, and wave functions were converged to within 10^{-4} eV. The maximum force on each atom was converged to <0.5 eV $Å^{-1}$. These protocols provided an estimate of the reaction path and starting points for the structure and the reactive mode for each transition state. The dimer algorithm was then used with wave functions converged to within 10^{-6} eV, and the maximum force on each atom was converged to <0.05 eV $Å^{-1}$.

Frequency calculations were performed on all optimized adsorbed species (all catalyst atoms were fixed) to estimate enthalpies (H) and free energies (G) for all reactants, products, and transition states at 543 K. For gaseous molecules, translational and rotational enthalpies and free energies were also computed from statistical mechanics. DFT-derived intrinsic enthalpy and free energy barriers (ΔH_{act} and ΔG_{act}, respectively) and reaction energies (ΔH_{rxn} or ΔG_{rxn}) denote differences between a transition state or the product and the precursor reactant for that elementary step. Overall barriers ($\Delta H^{\ddagger}$ and $\Delta G^{\ddagger}$) are defined as the enthalpy or free energy of forming the partially dehydrogenated transition state $[C_5H_{(10-\lambda/2)}O^{*\ddagger}]$ and a stoichiometric amount of gas-phase H_2 from gas-phase MTHF ($C_5H_{10}O$) and a bare surface

$$C_5H_{10}O(g) + * \rightarrow [C_5H_{(10-\lambda/2)}O^{*\ddagger}] + \lambda H_2(g) \quad (10)$$

$$\Delta H^{\ddagger} = H^{\ddagger} + \lambda H_{H2} - H_{MTHF} - H_{*} \quad (11)$$

$$\Delta G^{\ddagger} = G^{\ddagger} + \lambda G_{H2} - G_{MTHF} - G_{*} \quad (12)$$

Further details of the computational methods and equations for zero-point vibrational energies (ZPVE), H_{vib}, and G_{vib} from vibrational frequencies and H_{trans}, H_{rot}, G_{trans}, and G_{rot} for gas-phase molecules are reported in the SI (Section S3.3.2).

■ ASSOCIATED CONTENT

Supporting Information

The Supporting Information is available free of charge on the ACS Publications website at DOI: 10.1021/acscatal.7b04403.

DOI: 10.1021/acscatal.7b04403
ACS Catal. 2018, 8, 7141−7157

XRD diffractograms, CO adsorption isotherms, temperature-programmed reduction profiles, FTIR spectra, TEM images and nanoparticle size distributions, product selectivity distributions, approach to equilibrium, measured rate parity plot, predicted transition-state structures, free energy reaction coordinate diagrams, *k*-point mesh, deactivation profiles, and error propagation analysis (PDF)

AUTHOR INFORMATION

Corresponding Authors

*E-mail: hibbitts@ufl.edu.
*E-mail: dwflhrty@illinois.edu.

ORCID

Megan E. Witzke: 0000-0003-1204-6711
David D. Hibbitts: 0000-0001-8606-7000
David W. Flaherty: 0000-0002-0567-8481

Notes

The authors declare no competing financial interest.

ACKNOWLEDGMENTS

We thank Mark Triezenberg for assistance with catalyst synthesis and experiments. TEM and XRD measurements were carried out in part in the Frederick Seitz Materials Research Laboratory Central Research Facilities, University of Illinois. This material is based upon work supported by the National Science Foundation Graduate Research Fellowship Program under Grant No. DGE-1144245 and a TechnipFMC Educational Fund Fellowship at the University of Illinois. A.A. acknowledges Saudi Arabian Cultural Mission (SACM) and King Faisal University, Saudi Arabia, for funding his graduate studies and research.

REFERENCES

(1) Carpenter, D.; Westover, T. L.; Czernik, S.; Jablonski, W. Biomass feedstocks for renewable fuel production: a review of the impacts of feedstock and pretreatment on the yield and product distribution of fast pyrolysis bio-oils and vapors. *Green Chem.* **2014**, *16*, 384−406.

(2) Zeng, Y. N.; Zhao, S.; Yang, S. H.; Ding, S. Y. Lignin plays a negative role in the biochemical process for producing lignocellulosic biofuels. *Curr. Opin. Biotechnol.* **2014**, *27*, 38−45.

(3) Saidi, M.; Samimi, F.; Karimipourfard, D.; Nimmanwudipong, T.; Gates, B. C.; Rahimpour, M. R. Upgrading of lignin-derived bio-oils by catalytic hydrodeoxygenation. *Energy Environ. Sci.* **2014**, *7*, 103−129.

(4) Furimsky, E. Catalytic hydrodeoxygenation. *Appl. Catal., A* **2000**, *199*, 147−190.

(5) Chia, M.; Pagan-Torres, Y. J.; Hibbitts, D.; Tan, Q. H.; Pham, H. N.; Datye, A. K.; Neurock, M.; Davis, R. J.; Dumesic, J. A. Selective hydrogenolysis of polyols and cyclic ethers over bifunctional surface Sites on rhodium-rhenium catalysts. *J. Am. Chem. Soc.* **2011**, *133*, 12675−12689.

(6) Holladay, J. E.; White, J. F.; Bozell, J. J.; Johnson, D. *Top value-added chemicals from biomass*; U.S. Department of Energy, Battelle: Pacific Northwest National Laboratory, 2007; Vol. *II* (Results of Screening for Potential Candidates from Biorefinery Lignin).

(7) Alonso, D. M.; Bond, J. Q.; Dumesic, J. A. Catalytic conversion of biomass to biofuels. *Green Chem.* **2010**, *12*, 1493−1513.

(8) Prins, R.; Bussell, M. E. Metal phosphides: Preparation, characterization and catalytic reactivity. *Catal. Lett.* **2012**, *142*, 1413−1436.

(9) Oyama, S. T. Novel catalysts for advanced hydroprocessing: transition metal phosphides. *J. Catal.* **2003**, *216*, 343−352.

(10) Abu, I. I.; Smith, K. J. HDN and HDS of model compounds and light gas oil derived from Athabasca bitumen using supported metal phosphide catalysts. *Appl. Catal., A* **2007**, *328*, 58−67.

(11) Bui, P.; Cecilia, J. A.; Oyama, S. T.; Takagaki, A.; Infantes-Molina, A.; Zhao, H. Y.; Li, D.; Rodriguez-Castellon, E.; Jiménez Lopez, A. J. Studies of the synthesis of transition metal phosphides and their activity in the hydrodeoxygenation of a biofuel model compound. *J. Catal.* **2012**, *294*, 184−198.

(12) Bowker, R. H.; Smith, M. C.; Pease, M. L.; Slenkamp, K. M.; Kovarik, L.; Bussell, M. E. Synthesis and hydrodeoxygenation properties of Ruthenium Phosphide Catalysts. *ACS Catal.* **2011**, *1*, 917−922.

(13) Oyama, S. T.; Gott, T.; Zhao, H. Y.; Lee, Y. K Transition metal phosphide hydroprocessing catalysts: A review. *Catal. Today* **2009**, *143*, 94−107.

(14) Liu, P.; Rodriguez, J. A. Catalytic properties of molybdenum carbide, nitride and phosphide: a theoretical study. *Catal. Lett.* **2003**, *91*, 247−252.

(15) Peroni, M.; Mancino, G.; Barath, E.; Gutierrez, O. Y.; Lercher, J. A. Bulk and gamma-Al_2O_3-supported Ni_2P and MoP for hydrodeoxygenation of palmitic acid. *Appl. Catal., B* **2016**, *180*, 301−311.

(16) Cecilia, J. A.; Infantes-Molina, A.; Rodriguez-Castellon, E.; Jimenez-Lopez, A.; Oyama, S. T. Oxygen-removal of dibenzofuran as a model compound in biomass derived bio-oil on nickel phosphide catalysts: Role of phosphorus. *Appl. Catal., B* **2013**, *136-137*, 140−149.

(17) Zhao, H. Y.; Li, D.; Bui, P.; Oyama, S. T. Hydrodeoxygenation of guaiacol as model compound for pyrolysis oil on transition metal phosphide hydroprocessing catalysts. *Appl. Catal., A* **2011**, *391*, 305−310.

(18) Wu, S. K.; Lai, P. C.; Lin, Y. C. Atmospheric hydrodeoxygenation of guaiacol over nickel phosphide catalysts: Effect of phosphorus composition. *Catal. Lett.* **2014**, *144*, 878−889.

(19) Li, K. L.; Wang, R. J.; Chen, J. X. Hydrodeoxygenation of anisole over silica-supported Ni_2P, MoP, and NiMoP Catalysts. *Energy Fuels* **2011**, *25*, 854−863.

(20) Cho, A.; Shin, J.; Takagaki, A.; Kikuchi, R.; Oyama, S. T. Ligand and ensemble effects in bimetallic NiFe phosphide catalysts for the hydrodeoxygenation of 2-methyltetrahydrofuran. *Top. Catal.* **2012**, *55*, 969−980.

(21) Chen, J. X.; Yang, Y.; Shi, H.; Li, M. F.; Chu, Y.; Pan, Z. Y.; Yu, X. B. Regulating product distribution in deoxygenation of methyl laurate on silica-supported Ni-Mo phosphides: Effect of Ni/Mo ratio. *Fuel* **2014**, *129*, 1−10.

(22) Rensel, D. J.; Rouvimov, S.; Gin, M. E.; Hicks, J. C. Highly selective bimetallic FeMoP catalyst for C-O bond cleavage of aryl ethers. *J. Catal.* **2013**, *305*, 256−263.

(23) Oyama, S. T.; Onkawa, T.; Takagaki, A.; Kikuchi, R.; Hosokai, S.; Suzuki, Y.; Bando, K. K. Production of phenol and cresol from guaiacol on nickel phosphide catalysts supported on acidic supports. *Top. Catal.* **2015**, *58*, 201−210.

(24) Shi, H.; Chen, J. X.; Yang, Y.; Tian, S. S. Catalytic deoxygenation of methyl laurate as a model compound to hydrocarbons on nickel phosphide catalysts: Remarkable support effect. *Fuel Process. Technol.* **2014**, *118*, 161−170.

(25) Wu, S. K.; Lai, P. C.; Lin, Y. C.; Wan, H. P.; Lee, H. T.; Chang, Y. H. Atmospheric hydrodeoxygenation of guaiacol over alumina-, zirconia-, and silica-supported nickel phosphide catalysts. *ACS Sustainable Chem. Eng.* **2013**, *1*, 349−358.

(26) Moon, J. S.; Kim, E. G.; Lee, Y. K. Active sites of Ni_2P/SiO_2 catalyst for hydrodeoxygenation of guaiacol: A joint XAFS and DFT study. *J. Catal.* **2014**, *311*, 144−152.

(27) Bui, P. P.; Oyama, S. T.; Takagaki, A.; Carrow, B. P.; Nozaki, K. Reactions of 2-methyltetrahydropyran on silica-supported nickel phosphide in comparison with 2-methyltetrahydrofuran. *ACS Catal.* **2016**, *6*, 4549−4558.

DOI: 10.1021/acscatal.7b04403
ACS Catal. 2018, 8, 7141−7157

(28) Cho, A.; Kim, H.; Iino, A.; Takagaki, A.; Oyama, S. T. Kinetic and FTIR studies of 2-methyltetrahydrofuran hydrodeoxygenation on Ni_2P/SiO_2. *J. Catal.* **2014**, *318*, 151−161.
(29) Cho, A.; Takagaki, A.; Kikuchi, R.; Oyama, S. T. Active sites in Ni_2P/USY catalysts for the hydrodeoxygenation of 2-methyltetrahydrofuran. *Top. Catal.* **2015**, *58*, 219−231.
(30) Iino, A.; Cho, A.; Takagaki, A.; Kikuchi, R.; Oyama, S. T. Kinetic studies of hydrodeoxygenation of 2-methyltetrahydrofuran on a Ni_2P/SiO_2 catalyst at medium pressure. *J. Catal.* **2014**, *311*, 17−27.
(31) Romero, Y.; Richard, F.; Reneme, Y.; Brunet, S. Hydrodeoxygenation of benzofuran and its oxygenated derivatives (2,3-dihydrobenzofuran and 2-ethylphenol) over $NiMoP/Al_2O_3$ catalyst. *Appl. Catal., A* **2009**, *353*, 46−53.
(32) Engstrom, J. R.; Goodman, D. W.; Weinberg, W. H. Hydrogenolysis of ethane, propane, normal-butane, and neopentane on the (111) and (110)-(1 × 2) surfaces of iridium. *J. Am. Chem. Soc.* **1988**, *110*, 8305−8319.
(33) Flaherty, D. W.; Hibbitts, D. D.; Iglesia, E. Metal-catalyzed C-C bond cleavage in alkanes: Effects of methyl substitution on transition-state structures and stability. *J. Am. Chem. Soc.* **2014**, *136*, 9664−9676.
(34) Bond, G. C.; Cunningham, R. H. Alkane transformations on supported platinum catalysts 0.4. Kinetics of hydrogenolysis of ethane, propane, and n-butane on Pt/Al_2O_3 (EUROPT-3) and $PtRe/Al_2O_3$ (EUROPT-4). *J. Catal.* **1997**, *166*, 172−185.
(35) Gürbüz, E. I.; Hibbitts, D. D.; Iglesia, E. Kinetic and mechanistic asessment of alkanol/alkanal decarbonylation and deoxygenation pathways on metal catalysts. *J. Am. Chem. Soc.* **2015**, *137*, 11984−11995.
(36) Nakagawa, Y.; Tomishige, K. Production of 1,5-pentanediol from biomass via furfural and tetrahydrofurfuryl alcohol. *Catal. Today* **2012**, *195*, 136−143.
(37) McVicker, G. B.; Daage, M.; Touvelle, M. S.; Hudson, C. W.; Klein, D. P.; Baird, W. C.; Cook, B. R.; Chen, J. G.; Hantzer, S.; Vaughan, D. E. W.; Ellis, E. S.; Feeley, O. C. Selective ring opening of naphthenic molecules. *J. Catal.* **2002**, *210*, 137−148.
(38) Fahim, M. A.; AlSahhaf, T. A.; Elkilani, A. S. *Fundamentals of Petroleum Refining* **2010**, 1−496.
(39) Thompson, C. M.; Carl, L. M.; Somorjai, G. A. Sum frequency generation study of the interfacial layer in liquid-phase heterogeneously catalyzed oxidation of 2-propanol on platinum: Effect of the concentrations of water and 2-propanol at the Interface. *J. Phys. Chem. C* **2013**, *117*, 26077−26083.
(40) Aliaga, C.; Tsung, C. K.; Alayoglu, S.; Komvopoulos, K.; Yang, P. D.; Somorjai, G. A. Sum frequency generation vibrational spectroscopy and kinetic study of 2-methylfuran and 2,5-dimethylfuran hydrogenation over 7 nm patinum cubic nanoparticles. *J. Phys. Chem. C* **2011**, *115*, 8104−8109.
(41) Shurvell, H. F.; Southby, M. C. Infrared and Raman spectra of tetrahydrofuran hydroperoxide. *Vib. Spectrosc.* **1997**, *15*, 137−146.
(42) Surnev, L.; Xu, Z.; Yates, J. T. IRAS study of the adsorption of CO on Ni(111): Interrelation between various bonding modes of chemisorbed CO. *Surf. Sci.* **1988**, *201*, 1−13.
(43) Mihaylov, M.; Hadjiivanov, K.; Knozinger, H. Formation of $Ni(CO)_4$ during the interaction between CO and silica-supported nickel catalyst: an FTIR spectroscopic study. *Catal. Lett.* **2001**, *76*, 59−63.
(44) Chang, S. A.; Flaherty, D. W. Mechanistic study of formic acid decomposition over Ru(0001) and P_x-Ru(0001): Effects of phosphorus on C-H and C-O bond rupture. *J. Phys. Chem. C* **2016**, *120*, 25425−25435.
(45) Kiskinova, M.; Goodman, D. W. Modification of chemisorption properties by electronegative adatoms: -H_2 and CO on chlorided, sulfided, and phosphided Ni(100). *Surf. Sci.* **1981**, *108*, 64−76.
(46) Hibbitts, D.; Dybeck, E.; Lawlor, T.; Neurock, M.; Iglesia, E. Preferential activation of CO near hydrocarbon chains during Fischer−Tropsch synthesis on Ru. *J. Catal.* **2016**, *337*, 91−101.
(47) Layman, K. A.; Bussell, M. E. Infrared spectroscopic investigation of CO adsorption on silica-supported nickel phosphide catalysts. *J. Phys. Chem. B* **2004**, *108*, 10930−10941.
(48) Rodriguez, J. A.; Kim, J. Y.; Hanson, J. C.; Sawhill, S. J.; Bussell, M. E. Physical and chemical properties of MoP, Ni_2P, and MoNiP hydrodesulfurization catalysts: Time-resolved X-ray diffraction, density functional, and hydrodesulfurization activity studies. *J. Phys. Chem. B* **2003**, *107*, 6276−6285.
(49) Lee, Y. K.; Oyama, S. T. Bifunctional nature of a SiO_2-supported Ni_2P catalyst for hydrotreating: EXAFS and FTIR studies. *J. Catal.* **2006**, *239*, 376−389.
(50) Zaki, M. I.; Hasan, M. A.; Al-Sagheer, F. A.; Pasupulety, L. In situ FTIR spectra of pyridine adsorbed on SiO_2-Al_2O_3, TiO_2, ZrO_2 and CeO_2: general considerations for the identification of acid sites on surfaces of finely divided metal oxides. *Colloids Surf., A* **2001**, *190*, 261−274.
(51) Morterra, C.; Magnacca, G. A case study: Surface chemistry and surface structure of catalytic aluminas, as studied by vibrational spectroscopy of adsorbed species. *Catal. Today* **1996**, *27*, 497−532.
(52) Emeis, C. A. Determination of integrated molar extinction coefficients for infrared-absorption bands of pyridine adsorbed on solid acid catalysts. *J. Catal.* **1993**, *141*, 347−354.
(53) Abdelrahman, O. A.; Park, D. S.; Vinter, K. P.; Spanjers, C. S.; Ren, L.; Cho, H. J.; Vlachos, D. G.; Fan, W.; Tsapatsis, M.; Dauenhauer, P. J. Biomass-derived butadiene by dehydra-decyclization of tetrahydrofuran. *ACS Sustainable Chem. Eng.* **2017**, *5*, 3732−3736.
(54) Kumbhalkar, M. D.; Buchanan, J. S.; Huber, G. W.; Dumesic, J. A. Ring opening of biomass-derived cyclic ethers to dienes over silica/alumina. *ACS Catal.* **2017**, *7*, 5248−5256.
(55) Zhao, C.; He, J. Y.; Lemonidou, A. A.; Li, X. B.; Lercher, J. A. Aqueous-phase hydrodeoxygenation of bio-derived phenols to cycloalkanes. *J. Catal.* **2011**, *280*, 8−16.
(56) Zhao, C.; Kou, Y.; Lemonidou, A. A.; Li, X. B.; Lercher, J. A. Hydrodeoxygenation of bio-derived phenols to hydrocarbons using RANEY (R) Ni and Nafion/SiO_2 catalysts. *Chem. Commun.* **2010**, *46*, 412−414.
(57) Zhao, C.; Lercher, J. A. Selective hydrodeoxygenation of lignin-derived phenolic monomers and dimers to cycloalkanes on Pd/C and HZSM-5 Catalysts. *ChemCatChem* **2012**, *4*, 64−68.
(58) Abild-Pedersen, F.; Greeley, J.; Studt, F.; Rossmeisl, J.; Munter, T. R.; Moses, P. G.; Skulason, E.; Bligaard, T.; Nørskov, J. K. Scaling properties of adsorption energies for hydrogen-containing molecules on transition-metal surfaces. *Phys. Rev. Lett.* **2007**, *99*, 016105.
(59) Fernandez, E. M.; Moses, P. G.; Toftelund, A.; Hansen, H. A.; Martinez, J. I.; Abild-Pedersen, F.; Kleis, J.; Hinnemann, B.; Rossmeisl, J.; Bligaard, T.; Nørskov, J. K. Scaling relationships for adsorption energies on transition metal oxide, sulfide, and nitride surfaces. *Angew. Chem., Int. Ed.* **2008**, *47*, 4683−4686.
(60) Ferrin, P.; Simonetti, D.; Kandoi, S.; Kunkes, E.; Dumesic, J. A.; Nørskov, J. K.; Mavrikakis, M. Modeling ethanol decomposition on transition metals: A combined application of scaling and Brønsted-Evans-Polanyi relations. *J. Am. Chem. Soc.* **2009**, *131*, 5809−5815.
(61) Wang, S.; Petzold, V.; Tripkovic, V.; Kleis, J.; Howalt, J. G.; Skulason, E.; Fernandez, E. M.; Hvolbaek, B.; Jones, G.; Toftelund, A.; Falsig, H.; Bjorketun, M.; Studt, F.; Abild-Pedersen, F.; Rossmeisl, J.; Nørskov, J. K.; Bligaard, T. Universal transition state scaling relations for (de)hydrogenation over transition metals. *Phys. Chem. Chem. Phys.* **2011**, *13*, 20760−20765.
(62) Liu, J. W.; Hibbitts, D.; Iglesia, E. Dense CO adlayers as enablers of CO hydrogenation turnovers on Ru surfaces. *J. Am. Chem. Soc.* **2017**, *139*, 11789−11802.
(63) Jiao, L.; Regalbuto, J. R. The synthesis of highly dispersed noble and base metals on silica via strong electrostatic adsorption: I. Amorphous silica. *J. Catal.* **2008**, *260*, 329−341.
(64) Moteki, T.; Flaherty, D. W. Mechanistic Insight to C−C bond formation and predictive models for cascade reactions among alcohols on Ca- and Sr-Hydroxyapatites. *ACS Catal.* **2016**, *6*, 4170−4183.
(65) Kresse, G.; Furthmuller, J. Efficiency of ab-initio total energy calculations for metals and semiconductors using a plane-wave basis set. *Comput. Mater. Sci.* **1996**, *6*, 15−50.

DOI: 10.1021/acscatal.7b04403
ACS Catal. 2018, 8, 7141−7157

(66) Kresse, G.; Furthmuller, J. Efficient iterative schemes for ab initio total-energy calculations using a plane-wave basis set. *Phys. Rev. B: Condens. Matter Mater. Phys.* **1996**, *54*, 11169−11186.
(67) Kresse, G.; Hafner, J. Ab-initio molecular-dynamics for open-shell transition-metals. *Phys. Rev. B: Condens. Matter Mater. Phys.* **1993**, *48*, 13115−13118.
(68) Kresse, G.; Hafner, J. Ab-initio molecular-dynamics simulation of the liquid-metal amorphous-semiconductor transition in germanium. *Phys. Rev. B: Condens. Matter Mater. Phys.* **1994**, *49*, 14251−14269.
(69) Kresse, G.; Joubert, D. From ultrasoft pseudopotentials to the projector augmented-wave method. *Phys. Rev. B: Condens. Matter Mater. Phys.* **1999**, *59*, 1758−1775.
(70) Blochl, P. E. Projector augmented-wave method. *Phys. Rev. B: Condens. Matter Mater. Phys.* **1994**, *50*, 17953−17979.
(71) Hammer, B.; Hansen, L. B.; Norskov, J. K. Improved adsorption energetics within density-functional theory using revised Perdew-Burke-Ernzerhof functionals. *Phys. Rev. B: Condens. Matter Mater. Phys.* **1999**, *59*, 7413−7421.
(72) Perdew, J. P.; Burke, K.; Ernzerhof, M. Generalized gradient approximation made simple. *Phys. Rev. Lett.* **1996**, *77*, 3865−3868.
(73) Zhang, Y. K.; Yang, W. T. Comment on "Generalized gradient approximation made simple.". *Phys. Rev. Lett.* **1998**, *80*, 890.
(74) Taylor, A. Lattice parameters of binary nickel cobalt alloys. *J. I. Met.* **1950**, *77*, 585−594.
(75) Larsson, E. An X-ray investigation of Ni-P system and crystal structures of NiP and NiP_2. *Ark. Kemi* **1965**, *23*, 335−365.
(76) Ren, J.; Wang, J.; Li, J.; Li, Y. Density functional theory study on crystal nickel phosphides. *J. Fuel Chem. Techno* **2007**, *35*, 458−464.
(77) Rundqvist, S.; Yhland, M.; Dahlbom, R.; Sjövall, J.; Theander, O.; Flood, H. X-ray investigations of Mn_3P, Mn_2P, and Ni_2P. *Acta Chem. Scand.* **1962**, *16*, 992−998.
(78) Vitos, L.; Ruban, A. V.; Skriver, H. L.; Kollar, J. The surface energy of metals. *Surf. Sci.* **1998**, *411*, 186−202.
(79) Moula, M. G.; Suzuki, S.; Chun, W. J.; Otani, S.; Oyama, S. T.; Asakura, K. The first atomic-scale observation of a $Ni_2P(0001)$ single crystal surface. *Chem. Lett.* **2006**, *35*, 90−91.
(80) Monkhorst, H. J.; Pack, J. D. Special points for Brillouin-zone integrations. *Phys. Rev. B* **1976**, *13*, 5188−5192.
(81) Klimes, J.; Bowler, D. R.; Michaelides, A. Van der Waals density functionals applied to solids. *Phys. Rev. B: Condens. Matter Mater. Phys.* **2011**, *83*, 195131.
(82) Langreth, D. C.; Lundqvist, B. I.; Chakarova-Kack, S. D.; Cooper, V. R.; Dion, M.; Hyldgaard, P.; Kelkkanen, A.; Kleis, J.; Kong, L. Z.; Li, S.; Moses, P. G.; Murray, E.; Puzder, A.; Rydberg, H.; Schroder, E.; Thonhauser, T. A density functional for sparse matter. *J. Phys.: Condens. Matter* **2009**, *21*, 084203.
(83) Grimme, S.; Ehrlich, S.; Goerigk, L. Effect of the Damping Function in Dispersion Corrected Density Functional Theory. *J. Comput. Chem.* **2011**, *32*, 1456−1465.
(84) Wellendorff, J.; Lundgaard, K. T.; Mogelhoj, A.; Petzold, V.; Landis, D. D.; Nørskov, J. K.; Bligaard, T.; Jacobsen, K. W. Density functionals for surface science: Exchange-correlation model development with Bayesian error estimation. *Phys. Rev. B: Condens. Matter Mater. Phys.* **2012**, *85*, 235149.
(85) Henkelman, G.; Jónsson, H. Improved tangent estimate in the nudged elastic band method for finding minimum energy paths and saddle points. *J. Chem. Phys.* **2000**, *113*, 9978−9985.
(86) Jónsson, H.; Mills, G.; Jacobsen, K. W. Nudged elastic band method for finding minimum energy paths of transitions. *Classical and Quantum Dynamics in Condensed Phase Simulations*; World Scientific, 2011, 385−404.
(87) Henkelman, G.; Jónsson, H. A dimer method for finding saddle points on high dimensional potential surfaces using only first derivatives. *J. Chem. Phys.* **1999**, *111*, 7010−7022.

DOI: 10.1021/acscatal.7b04403
ACS Catal. 2018, 8, 7141−7157